

Long term wide-band spectro-temporal studies of outbursting black hole candidate sources GX 339–4 and H 1743–322: AstroSat and NuSTAR results

U. Aneesha,¹* Santabrata Das,¹† Tilak B. Katoch² and Anuj Nandi³‡

¹Indian Institute of Technology Guwahati, Guwahati, 781039, India

²Department of Astronomy and Astrophysics, Tata Institute of Fundamental Research, Homi Bhabha Road, Colaba, Mumbai, 400005, India

³Space Astronomy Group, ISITE Campus, U. R. Rao Satellite centre, Outer Ring Road, Marathahalli, Bangalore, 560037, India

Accepted XXX. Received YYY; in original form ZZZ

ABSTRACT

We present a comprehensive spectro-temporal analyses of recurrent outbursting black hole sources GX 339–4 and H 1743–322 using available *AstroSat* and *NuSTAR* archival observations during 2016 – 2024. The nature of the outburst profiles of both sources are examined using long-term *MAXI/GSC* and *Swift/BAT* lightcurves, and *failed* as well as *successful* outbursts are classified. Wide-band (0.5 – 60 keV) spectral modelling with disc (diskbb) and Comptonized (nthcomp) components indicates that GX 339–4 transits from hard ($kT_{\text{bb}} = 0.12 - 0.77$ keV, $\Gamma_{\text{nth}} = 1.54 - 1.74$ and $L_{\text{bol}} = 0.91 - 11.56\% L_{\text{Edd}}$) to soft state ($kT_{\text{in}} [\approx kT_{\text{bb}}] = 0.82 - 0.88$ keV, $\Gamma_{\text{nth}} = 1.46 - 3.26$, $L_{\text{bol}} = 19.59 - 30.06\% L_{\text{Edd}}$) via intermediate state ($kT_{\text{in}} [\approx kT_{\text{bb}}] = 0.56 - 0.88$ keV, $\Gamma_{\text{nth}} = 1.76 - 2.66$, $L_{\text{bol}} = 2.90 - 16.09\% L_{\text{Edd}}$), whereas H 1743–322 transits from quiescent to hard state ($\Gamma_{\text{nth}} = 1.57 - 1.71$, $L_{\text{bol}} = 2.08 - 3.48\% L_{\text{Edd}}$). We observe type-B and type-C Quasi-periodic Oscillations (QPOs) in GX 339–4 with increasing frequencies (0.10 – 5.37 Hz) along with harmonics. For H 1743–322, prominent type-C QPOs are observed in frequency range 0.22 – 1.01 Hz along with distinct harmonics. Energy-dependent power spectral studies reveal that fundamental QPO and harmonics disappear beyond 20 keV in GX 339–4, whereas fundamental QPO in H 1743–322 persists up to 40 keV. We also observe that type-C QPO_{rms}% decreases with energy for both sources although such variations appear marginal for type-B QPOs. Additionally, we report non-monotonic behavior of photon index with plasma temperature and detection of annihilation line. Finally, we discuss the relevance of the observational findings in the context of accretion dynamics around black hole binaries.

Key words: accretion, accretion discs – black hole physics – radiation mechanisms: general – X-rays: binaries – stars: individual: GX 339–4 – stars: individual: H 1743–322.

1 INTRODUCTION

In black hole X-ray binaries (BH-XRBs), the black hole accretes matter from the companion star and the temperature of the accreted matter becomes significantly high to produce X-ray emission. Considering the long term source variability, XRBs are broadly classified as persistent or transient sources (Chen et al. 1997; Corral-Santana et al. 2016; Tetarenko et al. 2016). In the case of persistent sources, such as Cygnus X-1 (Kushwaha et al. 2021), LMC X-1 and LMC X-3 (Bhuvana et al. 2021, 2022, and references therein), the central BH is steadily fed by the companion winds resulting the stable bolometric luminosity. On the other hand, black hole X-ray transients (BH-XRTs) are the low-mass X-ray binaries (LMXBs) harbouring an accreting BH that orbits with a low-mass ($\lesssim 2 M_{\odot}$) companion star. BH-XRTs are faint objects that mostly remain in the quiescent state ($L_{\text{x}} \sim 10^{31-33} \text{ erg s}^{-1}$) and accrete matter at very low rate (Tanaka & Lewin 1995; McClintock & Remillard 2006). However, bright

outbursts are occasionally triggered in BH-XRTs (GX 339–4 and H 1743–322), which usually last for hundreds of days and the source luminosity increases to $L_{\text{x}} \sim 10^{36-39} \text{ erg s}^{-1}$ (Corral-Santana et al. 2016; Tetarenko et al. 2016). Note that the transient LMXBs like GRS 1915+105 sustains outburst for an extended period (over 25 years) and hence are classified as persistent-cum-aperiodic variable source (Belloni et al. 2000; Nandi et al. 2001; Sreehari et al. 2020; Athulya et al. 2022; Majumder et al. 2022; Athulya & Nandi 2023, and references therein).

The energy spectra of BH-XRTs often consist of a thermal emission component originating from the accretion disc (Makishima et al. 1986; Mitsuda et al. 1984), and a non-thermal component resulted due to the inverse-Comptonisation (Sunyaev & Titarchuk 1980; Titarchuk 1994; Chakrabarti & Titarchuk 1995) of soft photons by ‘hot’ corona (~ 100 keV). In addition, BH-XRBs display rapid X-ray timing variabilities that are commonly examined by analysing the power density spectrum (PDS) (van der Klis 1989). The PDS often exhibits Quasi-periodic Oscillation (QPO; see Ingram & Motta 2019, for a recent review) features along with a broad-band noise continuum. In particular, Low-Frequency QPOs (LFQPOs) are observed over a wide range of frequencies ranging from mHz to few

* E-mail: aneesha@iitg.ac.in

† E-mail: sbdas@iitg.ac.in

‡ E-mail: anuj@ursc.gov.in

tens of Hz and are classified as type-A, type-B and type-C QPOs, respectively (Wijnands et al. 1999; Homan et al. 2001; Remillard et al. 2002; Casella et al. 2005). Indeed, type-B and type-C LFQPOs are characteristically different indicating their different physical origin. On the contrary, type-A LFQPO is rarely observed and is poorly understood.

During an outburst, the BH-XRTs generally evolve through distinct spectral states, namely Low/Hard State (LHS), Hard-Intermediate State (HIMS), Soft-Intermediate State (SIMS), and High/Soft State (HSS). These states occupy different positions in the hardness intensity diagram (HID; Homan & Belloni 2005; McClintock & Remillard 2006; Belloni & Motta 2016; Nandi et al. 2012; Radhika & Nandi 2014; Sreehari et al. 2019b; Sreehari & Nandi 2021; Nandi et al. 2024)) and form a hysteresis loop (Miyamoto et al. 1995; Belloni et al. 2005; Nandi et al. 2018). For a *successful* outburst, a source transits through all the spectral states, otherwise it is categorized as a *failed* outburst (Tetarenko et al. 2016; Alabarta et al. 2021).

In a successful outburst, when the source accretes matter at very low rate, the emergent X-ray emissions yield quiescent state (QS). As the source transits to LHS, X-ray emissions are dominated by the high energy photons where the photon index (Γ) lies in the range of 1.5 – 1.6. In LHS, the PDS is dominated by the broad-band noise component with a maximum fractional rms amplitude of 30 – 50% (Homan et al. 2001) and usually type-C QPO features are observed. Next, the source makes transition to intermediate states (HIMS and SIMS), where the soft photon contribution becomes significant with $\Gamma \sim 1.7\text{--}2.5$, and the rms noise in the PDS becomes weaker (typically rms $\sim 5\text{--}20\%$). The intermediate states (HIMS and SIMS) are distinguished from each other due to their different timing properties (Belloni & Motta 2016). Note that the type-C QPOs are observed in the LHS and HIMS, whereas type-A and type-B QPOs are seen in SIMS (Belloni et al. 2005; Radhika & Nandi 2014; Radhika et al. 2016; Belloni & Motta 2016). Subsequently, the source transits to HSS (Homan et al. 2001; Belloni 2005; Remillard & McClintock 2006; Nandi et al. 2012; Radhika et al. 2016; Nandi et al. 2018), where the source becomes bright and the radiation spectrum is dominated by the thermal disc photons with steep photon index $\Gamma \sim 3$. In HSS, PDS displays powerlaw signature with rms less than 2 – 3%. Finally, the source returns back to LHS via intermediate states and subsequently fades into quiescence. Indeed, these changes of the spectro-temporal properties evidently indicate that the spectral state transition during the evolution of an outburst seems to be associated with the accretion geometry.

Being motivated with the unique outburst features of BH-XRTs, we intend to study the long term wide-band spectro-temporal properties of two LMXB sources, namely GX 339–4 and H 1743–322. The source GX 339–4 was discovered in 1973 by satellite OSO-7 (Markert et al. 1973) and the source undergoes regular outbursts in every 2 – 3 years (Sreehari et al. 2018). Since its discovery, the source has been studied extensively (Méndez & van der Klis 1997; Corbel et al. 2003; Hynes et al. 2003; Zdziarski et al. 2004; Belloni et al. 2005; Shaposhnikov & Titarchuk 2009; Nandi et al. 2012; Titarchuk & Seifina 2021). GX 339–4 is located at the sky position RA = $17^h 02^m 49^s .38$ and Dec = $-48^\circ 47' 23'' .2$. Meanwhile, the absorption lines study in near-IR (Heida et al. 2017) indicates the presence of a giant K-type companion confirming previous finding (Hynes et al. 2004; Muñoz-Darias et al. 2008). The mass and distance of the source are found as $8.28 - 11.89 M_\odot$ (Sreehari et al. 2019a) and $d = 8.4 \pm 0.9$ kpc (Parker et al. 2016). During the outburst, GX 339–4 was found to demonstrate fast spectral state transitions, where it traces all the four spectral states (Belloni et al. 2005; Debnath et al. 2010; Nandi et al. 2012). Further, the temporal studies of GX339–4

reveals the presence of type-A, type-B and type-C QPOs (Motta et al. 2011).

The transient LMXB source H 1743–322 (IGR J17464–3213 or XTE J17464–3213) is located in the sky at RA = $17^h 46^m 15^s .596$ and Dec = $-32^\circ 14' 00'' .860$ at a distance of 8.5 ± 0.8 kpc (Steiner et al. 2012). The companion star is believed to be a late-type main-sequence star (Chaty et al. 2015) and the mass of the BH primary is estimated as $11.21^{+1.65}_{-1.96} M_\odot$ (Molla et al. 2017; Tursunov & Kolos 2018). The brightest outburst of H 1743–322 was observed in 2003 (~ 100 cts s $^{-1}$ in RXTE/ASM) by RXTE and INTEGRAL (Steiner et al. 2012; Homan et al. 2005a; Remillard et al. 2006; Kalemci et al. 2006). Note that the source underwent multiple outbursts with a recurrence period of 0.5 – 1 year after the 2003 outburst (Aneesha & Mandal 2020; Stiele & Yu 2016). H 1743–322 was found in all spectral states and the HID showed hysteresis pattern (Aneesha & Mandal 2020). Furthermore, this source exhibited high-frequency QPO (HFQPO) at 240 Hz during 2003 outburst (Homan et al. 2003) and mHz QPO at ~ 11 mHz during 2010 outburst (Altamirano & Strohmayer 2012).

In order to understand the underlying accretion scenarios during the outburst phases, in this paper, we analyse the spectro-temporal properties of GX 339–4 and H 1743–322 using the available archival *AstroSat* and *NuSTAR* data during 2016 – 2024. Broad-band spectral coverage along with excellent timing capabilities of *AstroSat* (Agrawal 2001) and *NuSTAR* (Harrison et al. 2013) allow us to investigate the nature of the accreting systems. Towards this, we examine the long term temporal variability of both sources using *MAXI/GSC* and *SWIFT/BAT* lightcurve. Further, in order to understand the overall nature of the outbursts, we examine HID of both sources. We conduct the wide-band spectral modelling that explains spectral characteristics of GX 339–4 and H 1743–322. We also performed a PDS analysis to examine the QPO features and observed that both sources exhibit type-B and/or type-C QPOs. With this, we perceive the nature of the accreting system present in the LMXBs under considerations.

The plan of the paper is as follows. In §2, we describe the observations and data reduction techniques. We discuss outburst profile and HID of outbursts for both sources in §3. We present the results of the spectral analysis in §4. In §5, we carry out the timing analysis. In §6, we present discussion and finally conclude.

2 OBSERVATION AND DATA REDUCTION

We analyse the publicly available observations of GX 339–4 and H 1743–322 from *AstroSat* and *NuSTAR* during 2016 – 2024. *AstroSat* data are obtained from Indian Space Research Organisation’s (ISRO’s) archival web-page¹ hosted at Indian Space Science Data Center (ISSDC). The *NuSTAR* data are publicly available at HEASARC website. All the observations under considerations are listed in Table 1. We make use of *MAXI* data obtained from *MAXI/GSC* on-demand web interface to depict the long term variation of lightcurve and hardness ratio (HR). For comparative study of the outburst profiles and HID of both sources, we utilize *MAXI/GSC* data. We also use *Swift/BAT* data to study the long term evolution of the lightcurves.

¹ https://astrobrowse.issdc.gov.in/astro_archive/archive/Home.jsp

Table 1. Details of *AstroSat* and *NuSTAR* observations of GX 339–4 and H 1743–322 during 2016 – 2024. Columns 1 – 9 denote Source name, Epoch, Observation ID, Mission Name, Obs. Date, *SXT* Exposure Time, *LAXPC* Exposure Time, *NuSTAR* Exposure Time, Hardness Ratio, respectively. Observations in quiescent phase are highlighted in light gray color. See the text for details.

Source	Epoch	Observation ID	Mission	Obs. Date (MJD)	Effective Exposure (ksec)			Hardness Ratio [†]	References	
					SXT	LAXPC	<i>NuSTAR</i>			
GX 339–4	AS1.01	T01_031T01_9000000368	<i>AstroSat</i>	11/03/2016 (57458.54)	~ 6.3	~ 10.1	-	$1.83^{+0.19}_{-0.05}$		
	AS1.02	G05_253T01_9000000560	<i>AstroSat</i>	24/07/2016 (57593.40)	~ 39.1	~ 53.7	-	$1.13^{+0.09}_{-0.13}$		
	NU1.03	80302304002	<i>NuSTAR</i>	02/10/2017 (58028.15)	-	-	~ 21.5	$2.62^{+0.05}_{-0.98}$	1, 2	
	AS1.04	A04_109T01_9000001578	<i>AstroSat</i>	04/10/2017 (58030.88)	~ 5.6	~ 21.6	-	$2.54^{+0.16}_{-0.23}$	3, 4	
	NU1.05	80302304004	<i>NuSTAR</i>	25/10/2017 (58051.57)	-	-	~ 17.9	$2.69^{+0.02}_{-0.01}$	1, 2, 3	
	NU1.06	80302304005	<i>NuSTAR</i>	02/11/2017 (58059.89)	-	-	~ 18.9	$2.80^{+0.24}_{-0.13}$	1, 2, 3	
	NU1.07	80302304007	<i>NuSTAR</i>	30/01/2018 (58148.36)	-	-	~ 28.9	$2.62^{+0.15}_{-0.02}$	1, 2	
	NU1.08	90401369002	<i>NuSTAR</i>	19/12/2018 (58471.18)	-	-	~ 0.6	$2.08^{+1.27}_{-1.39}$		
	NU1.09	90401369004	<i>NuSTAR</i>	05/01/2019 (58488.63)	-	-	~ 3.6	$2.83^{+0.46}_{-0.83}$	1	
	AS1.10	A05_166T01_9000003192	<i>AstroSat</i>	22/09/2019 (58748.70)	~ 11.5	~ 34.5	-	$2.73^{+0.01}_{-0.01}$	4	
	NU1.11	90502356004	<i>NuSTAR</i>	29/12/2019 (58846.58)	-	-	~ 0.6	$0.35^{+0.05}_{-0.02}$		
	NU1.12	80502325002	<i>NuSTAR</i>	20/02/2020 (58899.13)	-	-	~ 18.0	$0.13^{+0.07}_{-0.07}$		
	NU1.13	80502325004	<i>NuSTAR</i>	29/02/2020 (58908.65)	-	-	~ 20.3	$0.13^{+0.05}_{-0.06}$		
	NU1.14	80502325006	<i>NuSTAR</i>	01/04/2020 (58940.53)	-	-	~ 21.6	$0.50^{+0.05}_{-0.09}$		
	NU1.15	80502325008	<i>NuSTAR</i>	20/04/2020 (58959.05)	-	-	~ 22.4	$2.43^{+0.23}_{-0.97}$		
	NU1.16	90702303001	<i>NuSTAR</i>	23/01/2021 (59237.91)	-	-	~ 25.0	$2.77^{+0.16}_{-0.02}$		
	NU1.17	90702303003	<i>NuSTAR</i>	05/02/2021 (59250.99)	-	-	~ 21.9	$2.58^{+0.03}_{-0.01}$		
	AS1.18	T03_275T01_9000004180	<i>AstroSat</i>	13/02/2021 (59258.04)	~ 10.6	~ 27.9	-	$2.06^{+0.05}_{-0.20}$		
	NU1.19	90702303005	<i>NuSTAR</i>	20/02/2021 (59265.42)	-	-	~ 20.9	$2.44^{+0.04}_{-0.01}$		
	AS1.20	T03_279T01_9000004218	<i>AstroSat</i>	02/03/2021 (59275.04)	~ 99.8	~ 43.6	-	$1.99^{+0.09}_{-0.54}$		
	AS1.21	T03_280T01_9000004222	<i>AstroSat</i>	05/03/2021 (59278.11)	~ 9.2	~ 2.1	-	$1.90^{+0.07}_{-0.14}$		
	AS1.22	T03_281T01_9000004224	<i>AstroSat</i>	05/03/2021 (59278.38)	~ 0.9	~ 1.8	-	$2.22^{+0.32}_{-0.29}$		
	AS1.23	T03_282T01_9000004226	<i>AstroSat</i>	05/03/2021 (59278.45)	~ 1.2	~ 1.4	-	$2.01^{+0.38}_{-0.14}$		
	NU1.24	90702303007	<i>NuSTAR</i>	07/03/2021 (59280.99)	-	-	~ 23.4	$2.35^{+0.03}_{-0.01}$		
	NU1.25	90702303009	<i>NuSTAR</i>	26/03/2021 (59299.50)	-	-	~ 15.8	$1.26^{+0.35}_{-0.01}$		
	AS1.26	T03_291T01_9000004278	<i>AstroSat</i>	30/03/2021 (59303.06)	~ 22.3	~ 36.5	-	$0.33^{+0.04}_{-0.10}$	5, 6, 7	
	AS1.27	T03_291T01_9000004278	<i>AstroSat</i>	31/03/2021 (59304.00)	~ 23.0	~ 42.4	-	$0.20^{+0.06}_{-0.02}$	5	
	AS1.28	T03_291T01_9000004278	<i>AstroSat</i>	01/04/2021 (59305.03)	~ 25.7	~ 40.9	-	$0.29^{+0.01}_{-0.03}$	5	
	NU1.29	90702303011	<i>NuSTAR</i>	01/04/2021 (59305.81)	-	-	~ 14.8	$0.29^{+0.09}_{-0.07}$		
	AS1.30	T03_291T01_9000004278	<i>AstroSat</i>	02/04/2021 (59306.04)	~ 23.8	~ 47.5	-	$0.27^{+0.07}_{-0.10}$	5	
	AS1.31	T03_291T01_9000004278	<i>AstroSat</i>	03/04/2021 (59307.50)	~ 19.9	~ 33.1	-	$0.25^{+0.01}_{-0.11}$	5	
	AS1.32	T03_291T01_9000004278	<i>AstroSat</i>	04/04/2021 (59308.00)	~ 22.5	~ 42.2	-	$0.22^{+0.10}_{-0.03}$	5	
	AS1.33	T03_291T01_9000004278	<i>AstroSat</i>	05/04/2021 (59309.02)	~ 27.6	~ 51.1	-	$0.35^{+0.05}_{-0.04}$	5	
	AS1.34	T03_291T01_9000004278	<i>AstroSat</i>	06/04/2021 (59310.33)	~ 14.8	~ 21.8	-	$0.15^{+0.05}_{-0.20}$	5	
	NU1.35	90702303013	<i>NuSTAR</i>	23/04/2021 (59327.82)	-	-	~ 20.1	$0.16^{+0.06}_{-0.09}$		
	NU1.36	80601302002	<i>NuSTAR</i>	04/05/2021 (59338.96)	-	-	~ 13.6	$0.11^{+0.04}_{-0.02}$		
	NU1.37	80601302004	<i>NuSTAR</i>	05/05/2021 (59339.42)	-	-	~ 4.1	0.11 ± 0.06		
	NU1.38	80601302006	<i>NuSTAR</i>	05/05/2021 (59339.62)	-	-	~ 2.4	$0.09^{+0.01}_{-0.02}$		
	NU1.39	80702316002	<i>NuSTAR</i>	10/10/2021 (59497.09)	-	-	~ 21.3	$2.36^{+0.30}_{-0.24}$		
	NU1.40	80702316004	<i>NuSTAR</i>	20/10/2021 (59507.08)	-	-	~ 21.3	$2.47^{+0.08}_{-0.07}$		
	NU1.41	80702316005	<i>NuSTAR</i>	02/11/2021 (59520.35)	-	-	~ 17.8	$2.47^{+0.02}_{-0.07}$		
	AS1.42	T05_051T01_9000005334	<i>AstroSat</i>	07/09/2022 (59829.51)	~ 17.3	~ 38.9	-	2.29 ± 0.03		
	AS1.43	T05_053T01_9000005338	<i>AstroSat</i>	09/09/2022 (59831.54)	~ 34.0	~ 86.9	-	$2.95^{+0.03}_{-0.06}$		
	NU1.44	80801341002	<i>NuSTAR</i>	11/09/2022 (59833.22)	-	-	~ 21.0	$2.71^{+0.05}_{-0.12}$		
	AS1.45	A12_099T01_9000005716	<i>AstroSat</i>	28/06/2023 (60123.00)	~ 32.2	~ 50.8	-	0.73 ± 0.04		
	NU1.46	91001302001	<i>NuSTAR</i>	19/01/2024 (60328.04)	-	-	~ 18.6	$0.89^{+0.02}_{-0.04}$		
	NU1.47	91001304002	<i>NuSTAR</i>	31/01/2024 (60340.54)	-	-	~ 17.3	$0.16^{+0.01}_{-0.02}$		
	NU1.48	91002306002	<i>NuSTAR</i>	14/02/2024 (60354.70)	-	-	~ 16.4	$0.20^{+0.03}_{-0.04}$		
	AS1.49	A05_166T01_9000006070	<i>AstroSat</i>	14/02/2024 (60354.74)	~ 28.6	~ 50.7	-	$0.14^{+0.02}_{-0.04}$		
	AS1.50 [‡]	A13_028T01_9000006122	<i>AstroSat</i>	10/03/2024 (60379.44)	-	~ 84.3	-	-		
	NU1.51 [‡]	80902342002	<i>NuSTAR</i>	11/03/2024 (60380.16)	-	-	~ 19.5	-		
	NU1.52 [‡]	80902342001	<i>NuSTAR</i>	11/03/2024 (60380.16)	-	-	~ 0.36	-		
	AS1.53	T05_187T01_9000006132	<i>AstroSat</i>	21/03/2024 (60390.00)	~ 16.9	~ 25.7	-	0.10 ± 0.02		
	AS2.01	T01_045T01_9000000364	<i>AstroSat</i>	09/03/2016 (57456.40)	~ 6.4	~ 11.6	-	$2.52^{+0.02}_{-0.04}$	8, 9	
	NU2.02	80202012002	<i>NuSTAR</i>	13/03/2016 (57460.07)	-	-	~ 65.9	2.55 ± 0.01	10	
	NU2.03	80202012004	<i>NuSTAR</i>	15/03/2016 (57462.282)	-	-	~ 65.7	$2.520^{+0.002}_{-0.001}$	10	
	AS2.04	G05_253T03_9000000562	<i>AstroSat</i>	26/07/2016 (57595.10)	~ 41.3	~ 58.4	-	$1.44^{+0.06}_{-0.06}$		
	H 1743–322	AS2.05	G05_144T01_9000000612	<i>AstroSat</i>	18/08/2016 (57618.62)	~ 6.9	~ 19.3	-	$1.38^{+0.08}_{-0.19}$	
	AS2.06	G07_039T01_9000001444	<i>AstroSat</i>	08/08/2017 (57973.32)	~ 12.5	~ 14.8	-	$2.040^{+0.040}_{-0.003}$	8	
	NU2.07	90401335002	<i>NuSTAR</i>	19/09/2018 (58380.11)	-	-	~ 38.5	$2.950^{+0.003}_{-0.002}$	11, 12	
	NU2.08	80202012006	<i>NuSTAR</i>	26/09/2018 (58387.36)	-	-	~ 65.7	3.040 ± 0.003	11, 12	

[†]Hardness Ratio is calculated as the ratio of photon flux in 6 – 20 keV to 3 – 6 keV from *LAXPC* and *NuSTAR* spectra. A model combination $\text{TBabs} \times (\text{diskbb} + \text{gaussian} + \text{smedge} \times \text{Nthcomp})$ is used for photon flux estimation in units of photons cm⁻² s⁻¹.

[‡]Data are not in public domain.

References: 1: Wang et al. (2020), 2: García et al. (2019), 3: Debnath et al. (2023), 4: Husain et al. (2022), 5: Jana et al. (2024), 6: Mondal et al. (2023), 7: Peirano et al. (2023), 8: Husain et al. (2023), 9: Chand et al. (2021), 10: Chand et al. (2020), 11: Wang et al. (2022a), 12: Stiele & Kong (2021a).

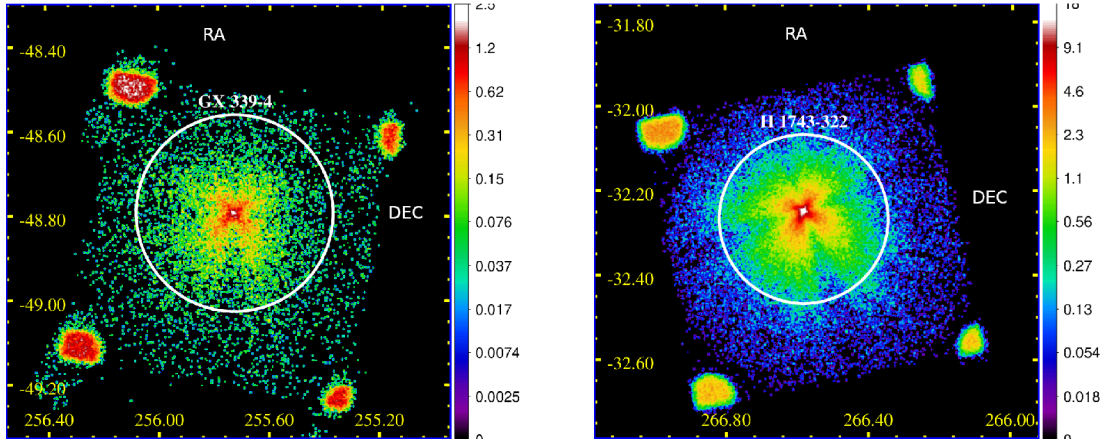


Figure 1. False color SXT image of GX 339–4 (left) during 4 October 2017 (MJD 58030.88) and H 1743–322 (right) during 8 August 2017 (MJD 57973.32). The image was generated from Photon Counting (PC) mode data. The image is smoothed out with a gaussian kernel of 3 pixel radius (1 pixel = 4.122 arcsec) using dS9. The four bright portions at the corners of the images are internal calibration sources which illuminate the corners of the CCD.

2.1 AstroSat/LAXPC

The LAXPC instrument on board *AstroSat* is a proportional counter operates in 3 – 80 keV energy range (Yadav et al. 2016; Antia et al. 2017). We use *LAXPC* Level-1 data in Event Analysis (EA) mode available in *AstroSat* public archive for timing and spectral analyses. We follow Sreehari et al. (2019a, 2020) for *LAXPC* data extraction procedure and analysis methods. We use the software LaxpcSoftv3.4² (Antia et al. 2017), released on June 14, 2021 to process the Level-1 data to Level-2 data. We combine *LAXPC10* and *LAXPC20* lightcurves for the timing studies, where 10 μ s temporal resolution of *LAXPC* data is used. Since *LAXPC10* has low gain and *LAXPC30* is not in working condition, we use data only from *LAXPC20* units for the spectral studies as it's gain remain stable throughout the entire observational period (Antia et al. 2021). Using GRPPHA, we group the *LAXPC* spectra to obtain the minimum count rate of 25 per bin.

2.2 AstroSat/SXT

The sources GX 339–4 and H 1743–322 were observed by the X-ray imaging instrument *SXT* on board *AstroSat*, which operates in 0.3 – 8 keV energy range. We obtain the Level-2 *SXT* data from the Indian Space Science Data Center (ISSDC) archive. The *SXT* data for all these sources are available in Photon Counting (PC) mode. The data reduction processes are performed following the procedures provided by *SXT* team at TIFR³. We use Julia based event merger tool (Julia_v01) to merge the individual orbit data. From the resultant cleaned event file, we generate images of both sources using XSELECT. We select a circular region of radius 12' around the source from which the source spectra and lightcurve were extracted (Sreehari et al. 2019a; Baby et al. 2021). The *SXT* image of GX 339–4 and H 1743–322 are presented in the left and right panels of Fig. 1. We check *SXT* images of the sources to find the count rate and follow the guidelines provided in *AstroSat* handbook⁴ for pile-up correction in our analysis. For both sources, we use background spectrum

and response provided by the *SXT* instrument team. The ancillary response file is created by SXTARFMODULE, which is provided by the *SXT* team. The *SXT* spectra is then grouped using GRPPHA to get the minimum count rate of 25 per bin.

2.3 NuSTAR

The *NuSTAR* is an X-ray telescope consisting of two detectors focal plane modules (FPMs), such as FPMA and FPMB, which operate in 3 – 79 keV energy range (Harrison et al. 2013). The *NuSTAR* instrument observed GX 339–4 and H 1743–322 on multiple epochs and the observation details are given in Table 1. To obtain the cleaned event file, we process the data using NUPipeline (version 0.4.8) available within HEASOFT and use the calibration database of CALDB version 20100101. XSELECT task is performed to select the source and background regions from cleaned event file. For source region, we select a circular region of radius 40'' centered at the peak brightness. The background is extracted from a region of same size away from the point source. We apply NUPRODUCTS task to generate the lightcurves, source spectra, background spectra along with their corresponding response matrices and ancillary responses.

2.4 MAXI/GSC and Swift/BAT

The Gas Slit Camera (GSC) on board Monitor of All-sky X-ray Image (*MAXI*) (Matsuoka et al. 2009; Nakahira et al. 2012) operates in 2–20 keV energy range, and the Burst Alert Telescope (BAT) on board Neil Gehrels Swift Observatory (*Swift*) (Gehrels et al. 2004; Krimm et al. 2013)) operates in 15 – 50 keV energy range. These two instruments continuously monitored GX 339–4 and H 1743–322. In this work, we make use of both *MAXI/GSC* and *Swift/BAT* lightcurves during 2016 – 2024. The one day averaged *MAXI/GSC* lightcurves of both sources are generated from *MAXI* on demand data publication system⁵. The *Swift/BAT* one day averaged lightcurves are downloaded from public archive⁶.

² http://www.tifr.res.in/~astrosat_laxpc/LaxpcSoft.html

³ https://www.tifr.res.in/~astrosat_sxt/dataanalysis.html

⁴ <https://www.issdc.gov.in/docs/as1/AstroSat-Handbook-v1.10.pdf>

⁵ <http://maxi.riken.jp/top/index.html>

⁶ <https://swift.gsfc.nasa.gov/results/transients/>

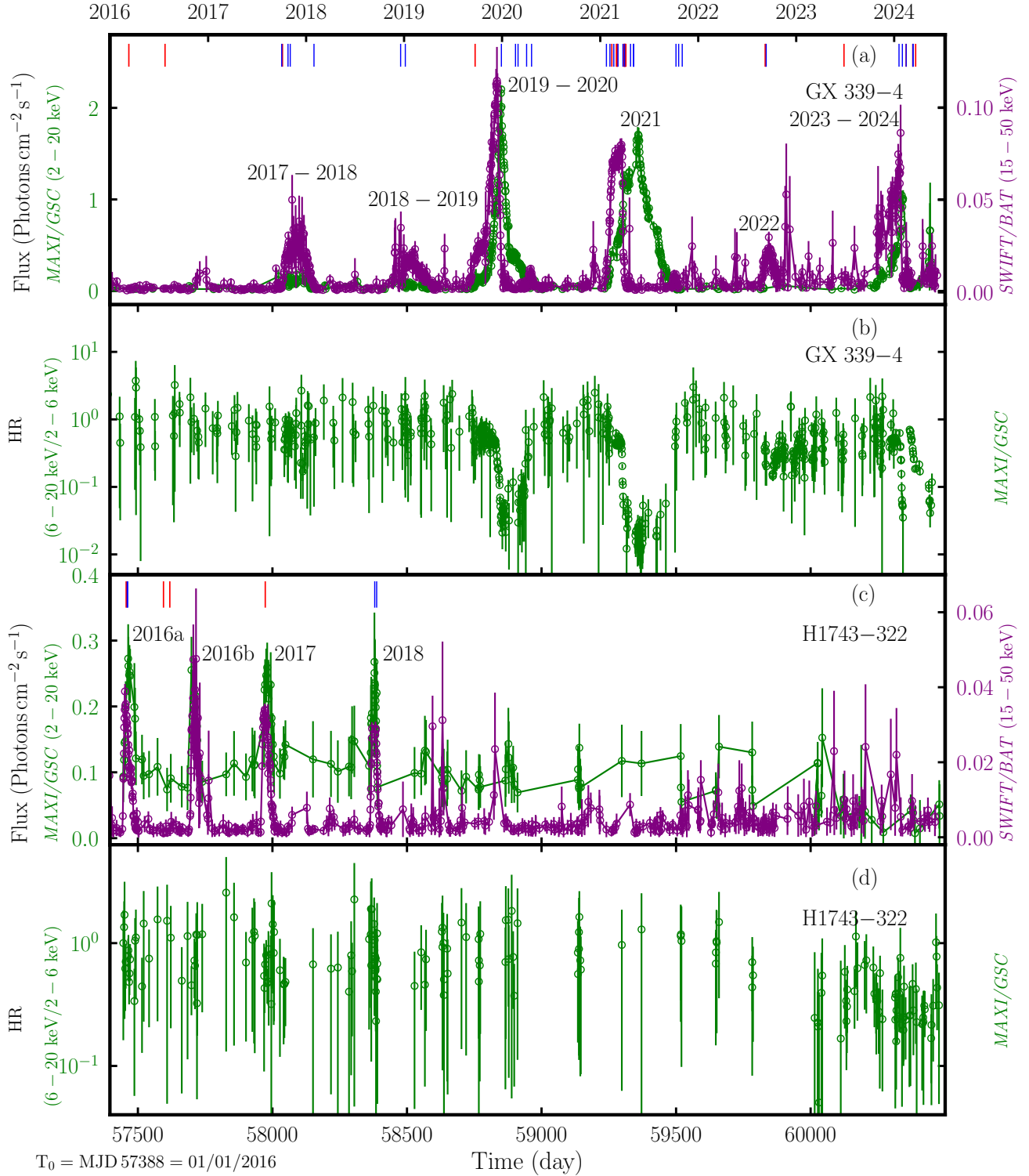


Figure 2. Variation of MAXI/GSC flux in 2 – 20 keV (open circles in green) and Swift/BAT flux in 15 – 50 keV (open circles in purple) with time (day) are shown for (a) GX 339–4 and (c) H 1743–322, respectively. The corresponding HR variations of GX 339–4 and H 1743–322 are presented in panel (b) and (d). Here, HR is calculated using photon flux (in units of $\text{photons cm}^{-2} \text{s}^{-1}$) values in different energy bands. Red and blue vertical bars denote AstroSat and NuSTAR observations. See the text for details.

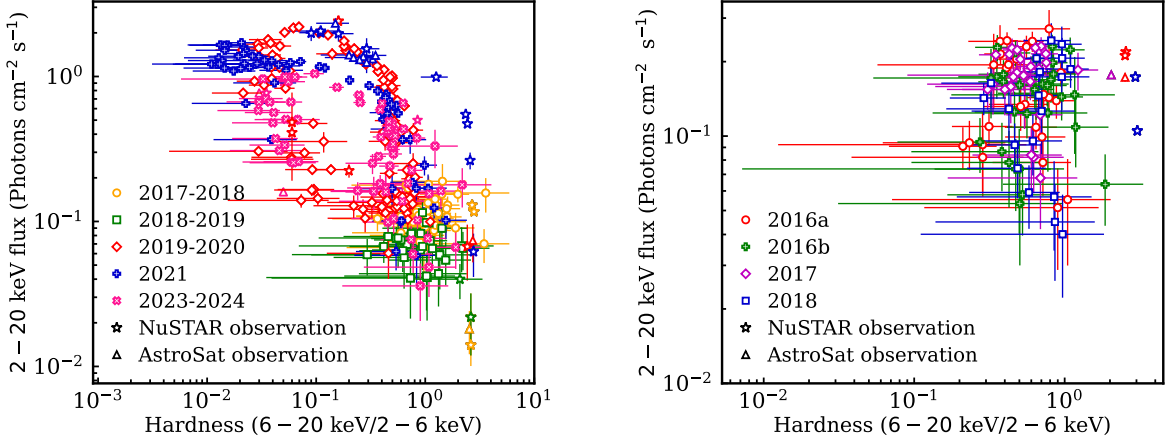


Figure 3. Hardness Intensity Diagram (HID) generated from *MAXI* data are presented for GX 339–4 (left panel) and H 1743–322 (right panel). Different outbursts are shown using different symbols as marked in each panel. Asterisk and triangle denote *AstroSat* and *NuSTAR* observations. See the text for details.

Table 2. Parameters of the outbursts of GX 339–4 and H 1743–322 from the *MAXI/GSC* data. From left to right (1) Outburst under study; (2) Start date of outburst; (3) End date of outburst; (4) Time taken for 2 – 6 keV, 6 – 20 keV and 2 – 20 keV lightcurve to reach the peak; (5) Peak flux in 2 – 6 keV, 6 – 20 keV and 2 – 20 keV lightcurve ; (6) Recurrence time; (7) Duration; (8) Outburst type. See the text for details.

Outburst	Start date (MJD)	End date (MJD)	T [†] _{peak}			F [★] _{peak}			T [□] _R T [⊗] _D		Type	
			days			Photons cm ⁻² s ⁻¹			days days			
			(2 – 6 keV)	(6 – 20 keV)	(2 – 20 keV)	(2 – 6 keV)	(6 – 20 keV)	(2 – 20 keV)	T [□] _R	T [⊗] _D		
GX 339–4												
2017-2018	06/09/2017 (58002)	02/04/2018 (58210)	42	42	42	0.18 ± 0.04	0.06 ± 0.01	0.18 ± 0.02	921	208	Failed	
2018-2019	23/12/2018 (58475)	25/04/2019 (58598)	30	7	7	0.08 ± 0.02	0.05 ± 0.02	0.10 ± 0.02	265	123	Failed	
2019-2020	04/09/2019 (58730)	31/05/2020 (59000)	115	95	115	2.24 ± 0.03	0.33 ± 0.02	2.20 ± 0.03	132	270	Successful	
2021	18/12/2020 (59201)	11/10/2021 (59498)	158	100	157	1.89 ± 0.08	0.21 ± 0.01	1.68 ± 0.03	201	297	Successful	
2022 [‡]	03/08/2022 (59794)	03/11/2022 (59886)	–	–	–	–	–	–	296	92	–	
2023-2024	10/10/2023 (60227)	10/04/2024(60410)	120	110	120	1.07 ± 0.07	0.24 ± 0.02	1.04 ± 0.05	341	183	Successful	
H 1743–322												
2016a	12/02/2016 (57430)	02/05/2016 (57510)	24	24	24	0.11 ± 0.06	0.08 ± 0.02	0.20 ± 0.04	191	80	Successful	
2016b	19/10/2016(57680)	31/01/2017 (57784)	24	26	24	0.17 ± 0.02	0.10 ± 0.02	0.24 ± 0.03	170	104	Failed	
2017	16/07/2017 (57950)	24/09/2017 (58020)	23	22	22	0.22 ± 0.03	0.12 ± 0.02	0.24 ± 0.04	166	70	Failed	
2018	19/09/2018 (58380)	19/10/2018 (58410)	8	8	8	0.12 ± 0.03	0.10 ± 0.03	0.24 ± 0.04	360	30	Failed	

[†] Time taken to reach peak flux in different energy bands.

★ The peak flux in different energy band.

□ The recurrence time (the time interval between the onset of this outburst and the end of the previous outburst).

⊗ The duration of outburst.

[‡] Lack of monitoring with *MAXI*

3 OUTBURST PROFILE AND HID

3.1 GX 339–4

During the *AstroSat* era starting from January 2016, GX 339–4 experienced six outbursts in 2017 – 2018, 2018 – 2019, 2019 – 2020, 2021, 2022 and 2023 – 2024 as shown in Fig. 2a. In Fig. 2b, we show the HR variation during all the outbursts including quiescent phases. We observe significant HR variability during 2019 – 2020, 2021 and 2023 – 2024 outbursts, whereas nearly steady HR variability (~ 1.3) is seen during 2017 – 2018, 2018 – 2019 and 2022 outbursts. In particular, we find that HR changes significantly from 1.2 to 0.01 during 2019 – 2020, 2021 and 2023 – 2024 outbursts indicating clear evidence of the spectral state transitions. This motivates us to carry out in-depth spectral analysis of this source presented in section 4.

In the left panel of Fig. 3, we present the HIDs of different outbursts generated from *MAXI/GSC* data for GX 339–4. We find that during

In this section, we examine the long term variability of lightcurves for GX 339–4 and H 1743–322 using *MAXI/GSC* and *SWIFT/BAT* data during 2016 – 2024. Towards this, in Fig. 2a and Fig. 2c, we show the lightcurves of GX 339–4 and H 1743–322, which are obtained from *MAXI/GSC* in 2 – 20 keV and *Swift/BAT* in 15 – 50 keV energy range. Using *MAXI/GSC* data, we calculate the hardness ratio (HR) defined as the ratio of photon counts in 6 – 20 keV to 2 – 6 keV, and plot it in Fig. 2b and Fig. 2d for GX 339–4 and H 1743–322, respectively.

2017 – 2018 and 2018 – 2019 outbursts, the source remained in the hard state without much variation of hardness. However, during 2019 – 2020, 2021 and 2023 – 2024 outbursts, the source underwent spectral state transition from hard state (initial phase) to soft state (peak of the outburst). The reverse trend is observed during the decay phase of both outbursts. Overall, we observe canonical ‘q’-shape in HID which is common in BH-XRBs (Nandi et al. 2012; Radhika et al. 2018; Sreehari et al. 2019b; Baby et al. 2021; Katoch et al. 2021; Prabhakar et al. 2022).

We generate *MAXI* lightcurves in 2 – 6 keV, 6 – 20 keV and 2 – 20 keV energy ranges for each outburst and compare the obtained results among different outbursts. The timing characteristics, such as peak flux, rising time, recurrence time and outburst duration determined from individual lightcurves are tabulated in Table 2. The 2017 – 2018 and 2018 – 2019 outbursts appeared less luminous ($F_{\text{peak}} \sim 0.2$ Photons cm $^{-2}$ s $^{-1}$ ~ 50 mCrab⁷) and have short duration ($T_D \sim 120$ days) compared to 2019 – 2020 and 2021 outbursts ($F_{\text{peak}} \sim 2$ Photons cm $^{-2}$ s $^{-1}$ ~ 530 mCrab and $T_D = 300$ days). Needless to mention that outbursts in 2017 – 2018 and 2018 – 2019 show shorter rising time ($T_{\text{peak}} \sim 7$ – 42 days) compared to 2019 – 2020, 2021 and 2023 – 2024 outbursts ($T_{\text{peak}} \sim 115$ – 157 days). We also find that 2 – 20 keV lightcurve lags 15 – 50 keV lightcurve typically by ~ 13 –58 days during 2018–2019, 2019–2020, 2021 and 2023–2024 outbursts, whereas no such time delay is observed during 2017–2018 outburst.

With the above considerations, we categorise 2017 – 2018 and 2018 – 2019 outbursts as *failed* one, and consider 2019 – 2020, 2021 and 2023 – 2024 outbursts as *successful* one. These findings are in agreement with the results reported earlier (García et al. 2019; Paice et al. 2019; Wang et al. 2020; Liu et al. 2021, 2022). However, we point out that 2022 outburst is not monitored continuously by *MAXI* and hence, it is not straightforward to understand whether the outburst was *successful* or *failed*.

3.2 H 1743–322

H 1743–322 displayed four outbursts, namely 2016a, 2016b, 2017 and 2018, during the period of 2016 – 2024 as shown in Fig. 2c. We present the HR variation in Fig. 2d, and find that HR does not show noticeable variations during the entire observation period. Further, we plot the HID in the right panel of Fig. 3 and observe insignificant HID evolution even in the 2016a successful outburst (Chand et al. 2020). We also carry out the spectral analysis of H 1743–322 to examine the spectral properties during the state transition as discussed in section 4.

Similar to GX 339–4, we perform the comparative analysis of outburst characteristics (*i.e.*, peak flux, rising time, recurrence time and outburst duration) of H 1743–322 and obtained results are tabulated in Table 2. All four outbursts yield similar peak flux $F_{\text{peak}} \sim 0.2$ Photons cm $^{-2}$ s $^{-1}$ ~ 50 mCrab with shorter rising time as well as smaller duration ($T_D \sim 30$ – 100 days). Note that we do not observe any time lag between lightcurves from 2 – 20 keV and 15 – 50 keV energy ranges.

4 SPECTRAL ANALYSIS AND RESULTS

We generate wide band energy spectra (0.7 – 60 keV) combining *SXT* (0.7 – 6 keV) and *LAXPC20* (4 – 60 keV) data of all *AstroSat*

⁷ 1 Crab = 3.8 Photons cm $^{-2}$ s $^{-1}$ in the 2 – 20 keV band of *MAXI/GSC*

observations for GX 339–4 and H 1743–322 sources. However, we consider spectral data upto 20 keV during the quiescent states of these sources. For *NuSTAR* observations, we use spectral data from FPMA in 3 – 60 keV energy band.

The spectral analysis is done using XSPEC V 12.11.1 (Arnaud 1996)) of HEASOFT V 6.28. We include 2% systematics (Sreehari et al. 2019a; Antia et al. 2021) for the spectral fitting of *AstroSat* observations. We incorporate gain corrections to all *SXT* and *LAXPC* fittings by using *gain fit* commands in XSPEC with fixed slope of 1 to correct the instrumental residue at 1.8 keV, and 2.2 keV. For few *SXT* observations, we simultaneously use both *gain fit* and *edge* models at 1.8 keV and 2.2 keV. While fitting the *LAXPC* spectra, we use *gain fit* and *gaussian* at ~ 30 keV to account for the Xenon edge arising from the instrument (Antia et al. 2017, 2021, 2022). Also, TBabs (Wilms et al. 2000) is used to account for the interstellar absorption of soft X-rays. We estimate the hydrogen column density N_H following Wilms et al. (2000). The relative cross-normalization between *SXT* and *LAXPC* is taken care by multiplying the model combination with a *constant*. The value of cross-normalization constant is set to unity for *SXT*, however, it is freely varied for *LAXPC* data, which is found as ~ 1 for most of the spectral fits.

The spectral modelling of GX 339–4 is carried out using basic thermal Comptonization model *Nthcomp* (Zdziarski et al. 1996; Źycki et al. 1999). In *Nthcomp* model, photon index Γ_{nth} , electron temperature (kT_e) and seed photon temperature (kT_{bb}) are treated as free parameters, and seed photons are modelled as multi-color disc blackbody (*diskbb*). For example, we fit the epoch AS1.01 (see Table 1) spectrum (using *Nthcomp*) which belongs to the quiescent state resulted in a comparatively good fit with $\chi^2_{\text{red}} = 1.24$ (54 dof). On the contrary, the spectral fitting of epoch AS1.04 (LHS) requires an additional *smedge* component at 6.9 keV leads to the acceptable fit with $\chi^2_{\text{red}} = 0.95$ (105 dof). Epoch AS1.26 belongs to intermediate state (IMS) which requires an additional thermal disc component *diskbb* along with *Nthcomp* and *smedge* for spectral fitting and good fit is obtained with $\chi^2_{\text{red}} = 1.13$ (595 dof). Similarly, we fit the *NuSTAR* spectrum (HSS; epoch NU1.35) using *diskbb*, *Nthcomp* and *gaussian* that resulted a good fit with $\chi^2_{\text{red}} = 1.04$ (542 dof). Note that we use $N_H = 0.5 \times 10^{22}$ atoms cm $^{-2}$ (Méndez & van der Klis 1997) while fitting the spectra. However, for few observations, we treat N_H as free parameter and find that $N_H \sim 0.40$ – 0.67×10^{22} atoms cm $^{-2}$.

In our spectral analyses, we employ a uniform model combination as *TBabs* \times (*diskbb*+*gaussian*+*smedge* \times *Nthcomp*) to compare the spectral model parameters in different spectral states. In reality, different spectral states are associated with the different accretion scenarios, and hence, alteration of the above model combination is often required based on a given spectral state. For example, *diskbb* component is required to describe the thermal emission during IMS and HSS of GX 339–4, whereas LHS is satisfactorily described without *diskbb* component. Notably, Fe line feature at 6.4 keV is prominently observed in *NuSTAR* spectra which is modelled with *gaussian* component. However, Fe line feature is hardly visible in *AstroSat* spectra possibly due to the poor resolution of the instrument, and *AstroSat* spectra are well fitted with *smedge* model component. Indeed, we find few exceptions, where additional *smedge* component is required for modelling the *NuSTAR* observations of GX 339–4. Note that the seed photon temperature (kT_{bb}) and inner disc temperature (kT_{in}) are tagged while modelling the combined spectra using *diskbb* and *Nthcomp* components. Following this, we carry out the spectral modelling of all the remaining observations in various epochs (see Table 1) and present the best fitted model parameters in Table 3. For the pur-

pose of representation, we depict the model fitted spectra of various spectral states of GX 339–4 in the left panel of Fig. 4.

We carry out the spectral analyses of H 1743–322 using the identical model combinations as used for GX 339–4 source. In epoch AS2.01, H 1743–322 was in LHS and the best fit spectral modelling is obtained using smedge component at 7.93 keV along with Nthcomp component, where $\chi^2_{\text{red}} = 1.07$ (500 dof). We fit *NuSTAR* spectrum (LHS, epoch NU2.02) using Nthcomp, gaussian at 6.25 keV and smedge around 8 keV to obtain an acceptable fit with $\chi^2_{\text{red}} = 1.02$ (1413 dof). However, during QS of *AstroSat* observation (epoch AS2.05), we fit the spectrum using Nthcomp and smedge around 7 keV that yields a good fit with $\chi^2_{\text{red}} = 1.35$ (45 dof). Similarly, we carry out the spectral modelling of all the observations and present the extracted model fitted parameters in Table 3. Note that for most of the observations, we treat N_{H} as free parameter yielding $N_{\text{H}} \sim 1.8 - 2.7 \times 10^{22} \text{ atoms cm}^{-2}$ for acceptable fit. We show the model fitted spectra of various states of H 1743–322 in the right panel of Fig. 4.

Using convolution model cflux in XSPEC, we estimate diskbb flux and Nthcomp flux in the energy range 0.7–50 keV. Similarly, we also compute the bolometric flux (F_{bol}) in 0.3–100 keV range and obtain the bolometric luminosity as $L_{\text{bol}} = F_{\text{bol}} \times 4\pi d^2$, where d is the source distance. We express L_{bol} in unit of Eddington luminosity (L_{Edd})⁸. We use system parameters as $M_{\text{BH}} = 9M_{\odot}$, $D = 8.5$ kpc (Parker et al. 2016) for GX 339–4 and $M_{\text{BH}} = 11.21M_{\odot}$ (Molla et al. 2017), $D = 8.5$ kpc (Steiner et al. 2012) for H 1743–322 to estimate the flux values and bolometric luminosity, which are summarized in Table 3.

In order to understand the nature of the Comptonizing medium in the vicinity of the source, we estimate the optical depth (τ) of the medium considering diffusion regime ($\tau \gg 1$). Following Lightman & Zdziarski (1987); Titarchuk & Lyubarskij (1995); Zdziarski et al. (1996), we calculate the spectral index α ($= \Gamma - 1$) which is given by,

$$\alpha = \left[\frac{9}{4} + \frac{1}{(kT_e/m_e c^2)\tau(1+\tau/3)} \right]^{1/2} - \frac{3}{2}, \quad (1)$$

where kT_e is the electron temperature, m_e is the electron mass, and c refers speed of light. We also estimate the Compton y-parameter (y-par) (see Agrawal et al. 2018; Chatterjee et al. 2021). For each observation under consideration, we tabulate both τ and y-par in Table 3.

4.1 GX 339–4

During *AstroSat* and *NuSTAR* observations, GX 339–4 underwent spectral transitions from quiescence to outburst phases and vice versa. We notice that during the outburst phases, the source transits between hard to soft states via intermediate states (IMS). The spectral modelling of different states results in $\tau \sim 1 - 12$. These findings infer the presence of optically thick corona surrounding the source. Moreover, we obtain y-par in the range 0.72–6.05. In the subsequent sections, we present the spectral properties of the source in different spectral states.

⁸ Eddington luminosity $L_{\text{Edd}} = 1.26 \times 10^{38} (M_{\text{BH}}/M_{\odot}) \text{ erg s}^{-1}$ for BH of mass M_{BH} (Frank et al. 2002).

4.1.1 Quiescent State (Epoch AS1.01-1.02, NU1.40-1.41, AS1.45)

During the five epochs of QS, the photon index (Γ_{nth}) varies in the range 1.71–2.48 and the corresponding HR value lies in between 1.13–2.47. This evidently indicates that the spectral nature of the source tends towards the harder state. From *NuSTAR* observations during epoch NU1.40 and NU1.41, the electron temperature kT_e is found to be 10.69 keV and 4.79 keV, respectively, whereas kT_e is kept frozen to 10 keV during *AstroSat* observations (see Table 3). Subsequently, we obtain Nthcomp flux as $(0.04 - 0.08) \times 10^{-9} \text{ erg cm}^{-2} \text{ s}^{-1}$, and the source luminosity (L_{bol}) is found to be low as $(0.03 - 0.06)\%L_{\text{Edd}}$ during quiescent phase.

4.1.2 Hard State (Epoch NU1.03, AS1.04, NU1.05-1.09, AS1.10, NU1.15-1.17, AS1.18, NU1.19, AS1.20-1.23, NU1.24, NU1.39, AS1.42-1.43, NU1.44, NU1.46)

GX 339–4 was observed in LHS during twenty three epochs of *AstroSat* and *NuSTAR*. Spectral analyses reveal that $\Gamma_{\text{nth}} \sim 1.54 - 1.74$ and hardness $\sim 0.89 - 2.95$. Moreover, we find that the seed photon temperature kT_{bb} varies as $\sim 0.12 - 0.77$ keV without any strong signature of disc emission, and $kT_e \sim 4.33 - 106.82$ keV. We observe Fe line feature comprising of the Gaussian width and normalisation that vary as 0.13–0.64 keV and $(0.09 - 1.02) \times 10^{-3} \text{ photons cm}^{-2} \text{ s}^{-1}$, respectively. We find that the Nthcomp flux is varied in the range $(0.27 - 10.32) \times 10^{-9} \text{ erg cm}^{-2} \text{ s}^{-1}$, and obtain $L_{\text{bol}} \sim (0.91 - 11.56)\%L_{\text{Edd}}$ which is significantly higher than QS state. The best fit spectral parameters are tabulated in Table 3.

4.1.3 Intermediate State (Epoch NU1.12-1.14, NU1.25, AS1.26-1.28, NU1.29, AS1.30-1.33, NU1.47-1.48, AS1.49, AS1.53)

AstroSat and *NuSTAR* observed GX 339–4 sixteen times in IMS which render $kT_{\text{in}} \sim 0.56 - 0.88$ keV signifying hotter disc, $\Gamma_{\text{nth}} \sim 1.76 - 2.66$ and HR $\sim 0.13 - 1.26$. In addition, electron temperature exhibits variation as $kT_e \sim 11.43 - 50.0$ keV. We find that the disc temperature reaches its maximum value ($kT_{\text{in}} \sim 0.88$ keV) during the epoch AS1.26. As in LHS, Fe line signature is also observed in IMS, however with stronger features having width as 0.60–1.02 keV and normalization as $(0.40 - 11.20) \times 10^{-3} \text{ photons cm}^{-2} \text{ s}^{-1}$. Further, we compute fluxes corresponding to diskbb and Nthcomp, which are obtained as $(2.47 - 16.21) \times 10^{-9} \text{ erg cm}^{-2} \text{ s}^{-1}$ and $(0.06 - 11.10) \times 10^{-9} \text{ erg cm}^{-2} \text{ s}^{-1}$, respectively. During IMS, the source luminosity is seen to vary in the range $L_{\text{bol}} \sim (2.90 - 16.09)\%L_{\text{Edd}}$. The details of extracted spectral fitted parameters are presented in Table 3.

4.1.4 Soft State (Epoch NU1.11, AS1.34, NU1.35-1.38)

During six epochs of *AstroSat* and *NuSTAR* observations, GX 339–4 was observed in HSS. We find $kT_{\text{in}} \sim 0.82 - 0.88$ keV and $\Gamma_{\text{nth}} \sim 1.46 - 3.26$. The corona temperature is found to vary between $kT_e \sim 1.63 - 32.36$ keV. We observe that the hardness ratio (see Table 2) varies as 0.09–0.35 confirming the source spectral nature as soft state. Notably, in HSS, we find Fe line signature as in IMS. The source luminosity is estimated as $L_{\text{bol}} \sim (19.59 - 30.06)\%L_{\text{Edd}}$, and the fluxes corresponding to diskbb and Nthcomp are $(17.40 - 26.06) \times 10^{-9} \text{ erg cm}^{-2} \text{ s}^{-1}$ and $(0.02 - 6.07) \times 10^{-9} \text{ erg cm}^{-2} \text{ s}^{-1}$, respectively. The model fitted and estimated parameters are mentioned in Table 3.

Table 3. Spectral parameters obtained from best fit modelling of GX 339–4 and H 1743–322 using *AstroSat* and *NuSTAR* observations during 2016 – 2024. A model combination $\text{TBabs} \times (\text{diskbb+gaussian+smedge+Nthcomp})$ is used for the spectral fitting of GX 339–4 and H 1743–322. The errors are quoted with 90% confidence. From left to right are (1) Epoch, (2) normalization constant for diskbb (3) electron temperature, (4) seed photon temperature, (5) power-law index, (6) Gaussian energy, (7) gaussian width, (8) gaussian normalisation, (9) smedge energy, (10) smearing width, (11) χ^2_{red} (χ^2/dof , dof = degree of freedom) (12) unabsorbed disc flux in 0.7 – 50 keV, (13) unabsorbed Nthcomp flux in 0.7 – 50 keV, (14) bolometric luminosity in 0.3 – 100 keV, (15) optical depth, (16) Compton y-parameter and (17) spectral states, respectively. See the text for details.

Epoch	Model fitted parameters										Estimated parameters					Spectral State	
	N_{diskbb} (km $^{-2}$)	kT_e (keV)	kT_{bb} (keV)	F_{nth}	E_{gaussian} (keV)	W_{gaussian} (keV)	Norm _{gaussian} $\times 10^{-3}$ Photons cm $^{-2}$ s $^{-1}$	E_{smedge} (keV)	W_{smedge} (keV)	χ^2_{red} (dof)	F_{diskbb} (0.7 – 50 keV) $\times 10^{-9}$ erg cm $^{-2}$ s $^{-1}$	F_{nth} (0.7 – 50 keV) $\times 10^{-9}$ erg cm $^{-2}$ s $^{-1}$	L_{bol} (0.3 – 100 keV) $\times 10^{30}$ erg s $^{-1}$	τ	y-par		
GX 339–4																	
AS1.01	–	10 †	0.30 \ddagger	2.10 $^{+0.10}_{-0.09}$	–	–	–	–	–	1.24 (54)	–	0.04	0.03	–	–	QS	
AS1.02	–	10 †	0.15 †	2.48 $^{+0.12}_{-0.12}$	–	–	–	–	–	1.32 (107)	–	0.05	–	–	–	QS	
NU1.03	–	27.54 $^{+9.68}_{-5.73}$	0.35 ± 0.95	1.66 $^{+0.03}_{-0.02}$	6.42 $^{+0.68}_{-0.10}$	0.19 ± 0.07	0.09 ± 0.02	–	–	1.06 (542)	–	0.27	2.78	4.2	2.68 ± 0.02	LHS	
AS1.04	–	50 †	0.14**	1.60 ± 0.04	–	–	–	6.90 $^{+1.03}_{-0.84}$	4.02 $^{+0.99}_{-0.78}$	0.95 (105)	–	0.45	4.32	–	–	LHS	
NU1.05	–	22.30 $^{+7.37}_{-5.56}$	0.213 ± 0.003	1.570 ± 0.003	6.33 ± 0.10	0.32 ± 0.26	0.25 ± 0.08	7.08 ± 0.09	5 †	1.10 (1292)	–	2.83	2.58	5	3.54 ± 0.10	LHS	
NU1.06	–	36.02 $^{+7.08}_{-5.59}$	0.214 ± 0.003	1.582 ± 0.007	6.39 $^{+0.12}_{-0.15}$	0.31 ± 0.08	0.5 ± 0.1	–	–	1.00 (1165)	–	2.43	2.68	4	3.37 ± 0.14	LHS	
NU1.07	–	30.34 $^{+7.02}_{-5.59}$	0.40 ± 0.006	1.64 $^{+0.02}_{-0.02}$	6.52 ± 0.07	0.38 ± 0.19	0.09 ± 0.03	–	–	1.10 (668)	–	0.43	4.39	3	2.73 ± 0.69	LHS	
NU1.08	–	4.33 ± 0.61	0.43 ± 0.03	1.74 $^{+0.08}_{-0.08}$	6.66 ± 0.30	0.36 ± 0.22	0.39 ± 0.18	–	–	1.34 (218)	–	0.51	4.16	9	3.33 ± 0.64	LHS	
NU1.09	–	19.89 $^{+3.18}_{-3.18}$	0.38 ± 0.01	1.57 $^{+0.09}_{-0.09}$	6.56 ± 0.13	0.34 $^{+0.15}_{-0.12}$	0.48 ± 0.14	–	–	1.33 (219)	–	1.56	1.81	5	3.64 ± 0.88	LHS	
AS1.10	–	33.18 ± 13.63	0.43 ± 0.03	1.543 ± 0.006	–	–	–	8.09 $^{+0.18}_{-0.10}$	2.00 ± 0.41	1.09 (480)	–	2.07	2.08	4	3.41 ± 1.40	LHS	
NU1.11	1634 $^{+67}_{-72}$	10 †	0.88 $^{+0.03}_{-0.03}$	2.69 ± 0.02	6.67 ± 0.12	4.0 †	4.49 ± 1.81	–	–	1.11 (293)	17.40	6.07	30.06	–	–	HSS	
NU1.12	2103 ± 521	50 †	0.66 ± 0.02	2.11 ± 0.07	6.40 ± 0.08	1.02 ± 0.04	1.87 ± 0.06	–	–	1.08 (540)	6.37	6.29	–	–	–	IMS	
NU1.13	2334 $^{+123}_{-101}$	50 †	0.64 ± 0.01	2.27 ± 0.01	6.40 $^{+0.18}_{-0.25}$	0.88 $^{+0.15}_{-0.12}$	1.61 ± 1.00	–	–	1.20 (417)	5.76	0.20	5.78	–	–	IMS	
NU1.14	1083 $^{+76}_{-88}$	50 †	0.63 ± 0.03	2.13 ± 0.02	6.02 ± 0.04	1.00 †	0.4 ± 0.1	–	–	1.13 (543)	2.47	0.52	2.90	–	–	IMS	
NU1.15	–	60.75 $^{+38.32}_{-37.32}$	0.355 ± 0.004	1.700 ± 0.002	6.39 ± 0.26	0.49 ± 0.13	0.23 ± 0.06	–	–	1.20 (918)	–	1.27	1.31	2	1.83 ± 0.53	LHS	
NU1.16	–	34.37 $^{+12.19}_{-12.19}$	0.22 ± 0.01	1.58 ± 0.01	6.45 $^{+0.06}_{-0.07}$	0.18 ± 0.08	0.20 ± 0.04	6.79 ± 0.31	0.20 †	0.98 (915)	–	1.32	1.45	3	2.81 ± 0.25	LHS	
NU1.17	–	32.45 $^{+2.88}_{-2.53}$	0.120 ± 0.003	1.613 ± 0.002	6.40 ± 0.09	0.13 ± 0.07	0.47 ± 0.10	7.36 ± 0.08	2 †	1.11 (1290)	–	5.41	5.70	3	2.86 ± 0.22	LHS	
AS1.18	–	18.11 $^{+3.37}_{-3.37}$	0.22 ± 0.01	1.675 ± 0.002	–	–	–	7.41 $^{+0.33}_{-0.27}$	4.41 ± 0.85	1.23 (544)	–	4.91	6.86	5	2.91 ± 0.38	LHS	
NU1.19	–	27.11 $^{+4.54}_{-2.85}$	0.203 ± 0.004	1.657 ± 0.001	6.48 ± 0.09	0.26 ± 0.09	1.02 ± 0.30	7.37 ± 0.09	5 †	1.06 (1165)	–	9.57	9.94	4	2.93 ± 0.10	LHS	
AS1.20	–	50 †	0.25 ± 0.07	1.65 ± 0.01	–	–	–	6.99 ± 0.10	5 †	1.23 (588)	–	4.00	9.13	–	–	LHS	
AS1.21	–	50 †	0.25 ± 0.15	1.666 ± 0.001	–	–	–	7.14 ± 0.11	5 †	1.30 (410)	–	5.91	6.88	–	–	LHS	
AS1.22	–	71.99 ± 14.21	0.25 ± 0.01	1.671 ± 0.003	–	–	–	6.97 ± 0.33	5 †	1.33 (339)	–	6.09	7.07	2	1.83 ± 0.37	LHS	
AS1.23	–	106.82 ± 19.06	0.16 ± 0.02	1.68 ± 0.01	–	–	–	6.94 ± 0.29	4.74 ± 0.33	1.15 (374)	–	6.78	6.95	1	1.46 ± 1.11	LHS	
NU1.24	–	39.27 ± 19.09	0.29 $^{+0.03}_{-0.05}$	1.68 $^{+0.17}_{-0.20}$	6.42 $^{+0.05}_{-0.07}$	0.27 ± 0.07	1.0 ± 0.2	7.32 ± 0.07	4.15 ± 1.98	1.19 (914)	–	10.32	11.56	3	2.28 ± 0.28	LHS	
NU1.25	1262 $^{+36}_{-25}$	50 †	0.61 ± 0.03	2.13 ± 0.02	6.09 ± 0.12	0.60 †	6.75 ± 0.23	7.71 ± 0.04	5 †	1.10 (916)	2.62	11.10	12.12	–	–	IMS	
AS1.26	1208 $^{+55}_{-55}$	50 †	0.879 $^{+0.03}_{-0.03}$	2.40 ± 0.04	–	–	–	7.67 $^{+0.26}_{-0.11}$	5 †	1.13 (595)	12.41	4.65	14.84	–	–	IMS	
AS1.27	1427 ± 33	50 †	0.84 ± 0.02	2.43 ± 0.14	–	–	–	7.61 ± 0.12	5 †	1.13 (583)	11.95	3.43	12.93	–	–	IMS	
AS1.28	–	1450 $^{+38}_{-38}$	50 †	0.84 ± 0.03	2.37 ± 0.05	–	–	7.81 ± 0.36	5 †	1.12 (598)	11.90	2.97	12.77	–	–	IMS	
NU1.29	2132 $^{+30}_{-30}$	50 †	0.81 $^{+0.04}_{-0.17}$	2.19 $^{+0.02}_{-0.03}$	6.40 ± 0.11	1.02 ± 0.04	11.2 ± 0.40	–	–	1.08 (542)	15.61	0.24	16.09	–	–	IMS	
AS1.30	1166 $^{+30}_{-43}$	50 †	0.83 ± 0.01	2.27 ± 0.04	–	–	–	7.45 ± 0.32	5 †	1.29 (596)	9.49	1.68	10.26	–	–	IMS	
AS1.31	1562 ± 12	11.43 $^{+4.19}_{-4.12}$	0.56 ± 0.03	2.17 ± 0.12	–	–	–	6.95 ± 0.32	5 †	1.18 (572)	13.69	3.07	14.17	4	1.39 ± 0.24	IMS	
AS1.32	1754 $^{+28}_{-28}$	50 †	0.56 $^{+0.12}_{-0.33}$	1.97 $^{+0.04}_{-0.05}$	–	–	–	6.71 ± 0.72	5 †	1.11 (582)	14.73	1.65	13.47	1	0.87 ± 0.08	IMS	
AS1.33	1712 $^{+37}_{-37}$	37.16 ± 9.62	0.8634 ± 0.0004	1.78 $^{+0.41}_{-0.41}$	–	–	–	7.89 ± 0.16	1.00 ± 0.003	1.14 (595)	16.21	0.06	14.89	1	1.06 ± 0.76	IMS	
AS1.34	2602 $^{+30}_{-30}$	16.78 $^{+0.31}_{-0.31}$	0.852 ± 0.003	1.82 $^{+0.13}_{-0.13}$	–	–	–	7.40 $^{+0.24}_{-0.32}$	5 †	1.18 (593)	26.06	0.08	22.60	4	2.21 ± 0.10	HSS	
NU1.35	2538 $^{+41}_{-39}$	32.36 ± 12.78	0.83 ± 0.01	1.99 $^{+0.03}_{-0.03}$	6.40 ± 0.11	0.78 ± 0.06	4.79 ± 0.60	–	–	1.04 (542)	20.09	0.82	19.59	2	1.30 ± 0.54	HSS	
NU1.36	2939 $^{+29}_{-29}$	5.18 $^{+0.18}_{-0.18}$	0.82 ± 0.03	1.46 $^{+0.23}_{-0.23}$	6.18 $^{+0.23}_{-0.23}$	0.78 $^{+0.21}_{-0.21}$	4.70 ± 0.23	–	–	1.14 (541)	22.95	0.02	20.88	12	6.05 ± 0.22	HSS	
NU1.37	2953 $^{+16}_{-16}$	5.79 $^{+0.24}_{-0.24}$	0.82 $^{+0.02}_{-0.02}$	1.75 $^{+0.05}_{-0.05}$	6.16 $^{+0.33}_{-0.33}$	0.6 $^{+0.16}_{-0.16}$	4.38 ± 0.06	–	–	1.10 (366)	23.25	0.03	21.26	8	3.13 ± 0.18	HSS	
NU1.38	2747 ± 16	1.63 $^{+0.07}_{-0.03}$	0.823 $^{+0.005}_{-0.002}$	3.26 ± 0.05	–	–	–	–	–	1.06 (173)	20.35	1.41	20.19	8	0.72 ± 0.04	HSS	
NU1.39	–	50	0.250 ± 0.003	1.698 ± 0.001	6.24 ± 0.21	0.64 ± 0.24	0.22 ± 0.08	–	–	1.08 (532)	–	0.88	0.91	–	–	LHS	
NU1.40	–	10.69 $^{+3.05}_{-1.87}$	0.12 †	1.71 ± 0.02	–	–	–	–	–	1.08 (495)	–	0.08	0.06	6	3.04 ± 0.06	QS	
NU1.41	–	47.79 $^{+60}_{-60}$	0.20 †	1.76 ± 0.01	–	–	–	–	–	1.07 (344)	–	0.06	0.04	8	3.17 ± 0.05	QS	
AS1.42	–	15.48 $^{+1.62}_{-1.62}$	0.57 $^{+0.01}_{-0.02}$	1.58 ± 0.01	–	–	–	8.02 ± 0.12	5 †	1.28 (529)	–	1.12	1.58	6	3.75 ± 0.28	LHS	
AS1.43	–	32.90 $^{+12.53}_{-11}$	0.773 ± 0.001	1.602 ± 0.011	–	–	–	7.75 ± 0.15	5 †	1.11 (527)	–	0.55	1.85	3	2.92 ± 0.12	LHS	
NU1.44	–	55.77 $^{+22}_{-22}$	0.33 ± 0.01	1.582 ± 0.001	6.34 $^{+0.11}_{-0.14}$	0.23 $^{+0.15}_{-0.14}$	0.34 ± 0.11	–	–	1.26 (752)	–	2.29	2.51	2	2.58 ± 0.30	LHS	
AS1.45	–	10 †	0.14 †	2.79 $^{+0.26}_{-0.23}$	–	–	–	–	–	1.02 (87)	–	0.01	0.01	–	–	QS	
NU1.46	–	24.98 $^{+2.22}_{-1.44}$	0.22 ± 0.08	1.722 ± 0.003	6.42 $^{+0.08}_{-0.08}$	0.34 ± 0.08	1.99 ± 0.34	7.62 ± 0.04	5 †	1.07 (1165)	–	9.02	9.61	4	2.41 ± 0.22	LHS	
NU1.47	1920 $^{+97}_{-90}$	50 †	0.80 ± 0.01	2.48 ± 0.03	6.17 ± 0.03	0.6 †	6.20 ± 0.60	7.98 ± 0.05	5 †	1.11 (791)	13.35	4.31	15.69	–			

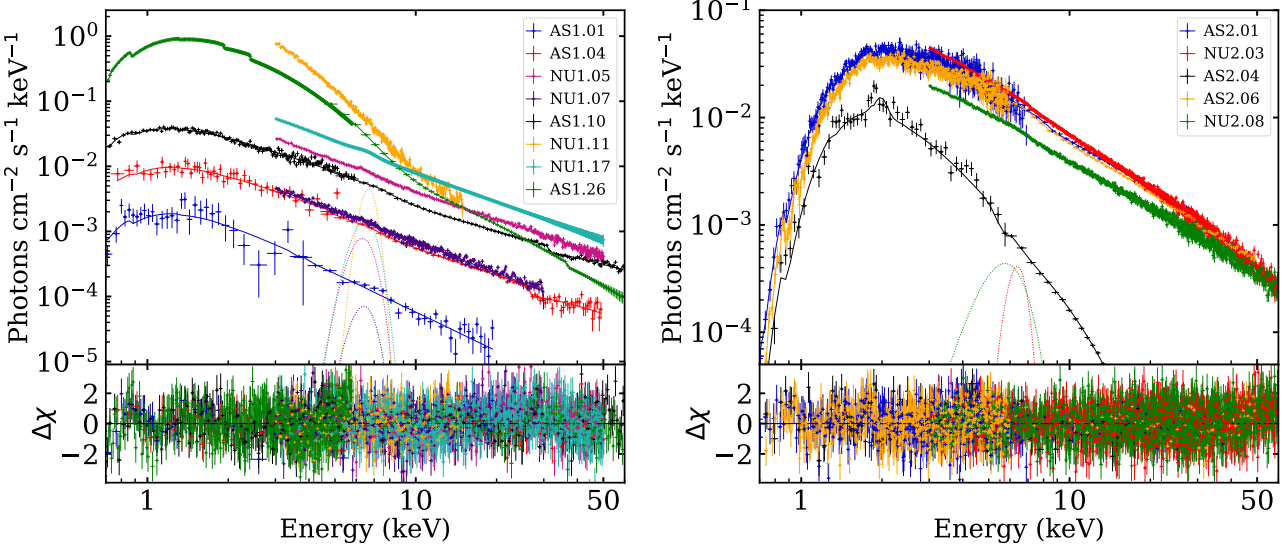


Figure 4. *Left panel:* Spectra of GX 339–4 during quiescence – AS1.01 (blue), hard – AS1.04 (red); NU1.05 (magenta); NU1.07 (navy blue); AS1.10 (black); NU1.17 (sky blue), intermediate – AS1.26 (green), and soft – NU1.11 (orange) states are shown. *Right panel:* Spectra of H 1743–322 during quiescence – AS2.04 (black), and hard – AS2.01 (blue); NU2.03 (red); AS2.06 (orange); NU2.08 (green) states are shown. Corresponding gaussian emission line components are also shown. In both figures, bottom panels show residual variation of spectral fitting. See the text for details.

4.2.2 Hard State (Epoch AS2.01, NU2.02, NU2.03, AS2.06, NU2.07, NU2.08)

AstroSat and *NuSTAR* observed H 1743–322 during six epochs in LHS. The spectral analyses of these observations yield $\Gamma_{\text{nth}} \sim 1.57 - 1.71$ along with $\text{HR} \sim 2.04 - 3.04$ signifying the hard spectral state. Note that we find weak signature of seed photon temperature $kT_{\text{bb}} \sim 0.25 - 0.96$ keV without any thermal disc component. We also observe Fe line feature at ~ 6.4 keV. We find that the source luminosity is enhanced compared to the QS as $L_{\text{bol}} \sim (2.08 - 3.48)\% L_{\text{Edd}}$. All the fitted and estimated parameters are summarized in Table 3.

5 TIMING ANALYSIS AND RESULTS

In order to examine the timing variability of GX 339–4 and H 1743–322, we generate PDS using 5 ms lightcurves in different energy bands of *LAXPC* (*LAXPC10* and *LAXPC20*) and *NuSTAR* (*FPMA* and *FPMB*) observations. We use *powspec* tool to generate PDS in 0.001–30 Hz frequency range. For GX 339–4 source, we divide *LAXPC* lightcurve into intervals of 8192 time bins and construct the PDS for each of these intervals. We generate Leahy-normalised PDS using these segments and eventually average them to obtain the final PDS. Further, the average PDS is binned geometrically by a factor of -1.02 in the frequency space. Similarly, for *NuSTAR* data, we divide the lightcurve into 16384 time bins and obtain the resultant PDS after re-binning geometrically by a factor of -1.03 . In case of H 1743–322, we divide both *LAXPC* and *NuSTAR* lightcurves into 8192 time bins and rebin the resultant PDS with a geometrical rebinning factor of -1.03 .

We carry out the model fitting of the PDS using a constant, zero-centered Lorentzian and Lorentzian to identify the QPO features (Belloni & Hasinger 1990). In doing so, we avoid correcting the Poisson noise contribution. The functional form of Lorentzian used in *XSPEC* is given by,

$$L(\nu) = \frac{K}{\pi} \frac{\Delta}{(\nu - \nu_c)^2 + \Delta^2}, \quad (2)$$

where ν is the frequency and ν_c is the central frequency representing the characteristic QPO frequency. Here, Δ is the half width at half maximum (HWHM) of the line and K is the normalization. For each observation describing QPO, we estimate ν_c , Δ , and K . Subsequently, we compute quality factor ($Q = \nu_c/2\Delta$) and significance (ratio of Lorentzian normalization to its negative error) (see Alam et al. 2014; Sreehari et al. 2019a, and references therein) that yield confirmed QPO detection provided $Q \geq 3$ and significance $\sigma \geq 3$. Further, the temporal variability in the lightcurve is parametrized by means of fractional root mean square (rms) variability. When PDS is Leahy normalised (Leahy et al. 1983), the fractional rms amplitude of each QPO is calculated as the square root of the definite integral of the Lorentzian representing the QPO in frequency–power space. Subsequently, the total rms of the PDS is calculated by integrating the Lorentzian over the entire frequency.

For GX 339–4, we fit the PDS obtained from *NuSTAR* observation during epoch NU1.19 using three Lorentzian and a constant that yields a positive residual around 0.13 Hz with $\chi^2_{\text{red}} = 1.54$ (223). Hence, we include an additional Lorentzian to account the QPO feature that renders $\chi^2_{\text{red}} = 1.37$ (223). Similarly, we fit the PDS of *AstroSat* observation during epoch AS1.26 with two Lorentzian and a constant that results residuals in the form of QPO near 2.86 Hz, 5.37 Hz and 9.83 Hz. Accordingly, we include three additional Lorentzian to model the QPO features and the best fit is obtained with $\chi^2_{\text{red}} = 1.18$ (174). We follow the same procedure to model PDS of other epochs as well. For H 1743–322, the PDS of epoch AS2.01 is modelled using one constant, two zero centroid Lorentzian and a Lorentzian around 0.14 Hz. In order to model QPO features around 0.60 Hz and 1.20 Hz, we add two additional Lorentzian around those frequencies that provides good fit with $\chi^2_{\text{red}} = 1.36$ (193). In addition, we model PDS generated from *NuSTAR* lightcurve of epoch NU2.02 with one Lorentzian and a constant. We add two Lorentzian to account the QPO feature around 0.95 Hz that gives $\chi^2_{\text{red}} = 4.64$ (113). In order to improve the fitting, we further include two additional Lorentzian around 0.18 Hz and 2.13 Hz and obtain $\chi^2_{\text{red}} = 0.94$ (107). We follow similar fitting routine for the remaining

Table 4. Details of the best fitted PDS parameters using *NuSTAR* and *LAXPC* observations of GX 339–4 and H 1743–322 during 2016 – 2024. PDS of both sources are fitted adopting a model combination $CO + \sum_{i=1}^6 L_i$, where CO denotes constant and L_i ($i = 1, 2, 3, 4, 5$ and 6) refers multiple Lorentzian used to obtain the best fit. σ_1 , σ_2 and σ_3 denote the significance of QPOs. QPO_{rms}% and Total_{rms}% represent the rms percentage of the QPO features and the entire PDS. The centroid frequency (LC) (in bold font), FWHM (LW) and normalization (LN) of the detected QPOs are mentioned. All errors are computed with 68% confidence. See the texts for details.

Epoch	CO	Model Parameters						Estimated Parameters									
		L ₁	L ₂	L ₃	L ₄	L ₅	L ₆	χ^2_{red} (dof)	σ_1	QPO _{rms1} %	σ_2	QPO _{rms2} %	σ_3	QPO _{rms3} %	Total _{rms} %	QPO type	
GX 339–4																	
AS1.01	2.05 ± 0.01	LC 0.0	—	—	—	—	—	0.91 (122)	—	—	—	—	—	—	2.82 ± 0.02	—	
	LW 1.852 ± 1.010	—	—	—	—	—	—	—	—	—	—	—	—	—	—	—	
	LN 0.09 ± 0.06	—	—	—	—	—	—	—	—	—	—	—	—	—	—	—	
AS1.02	2.062 ± 0.003	LC 0.0	0.42 ^{+0.09} _{-0.08}	—	—	—	—	—	1.31 (184)	—	—	—	—	—	—	9.93 ± 0.01	—
	LW 0.78 ± 0.10	0.62 ± 0.12	—	—	—	—	—	—	—	—	—	—	—	—	—	—	—
	LN 0.68 ± 0.14	0.43 ± 0.12	—	—	—	—	—	—	—	—	—	—	—	—	—	—	—
NU1.03	1.976 ± 0.003	LC 0.0	0.0	—	—	—	—	—	—	—	—	—	—	—	—	42.61 ± 0.001	—
	LW 1.04 ^{+0.16} _{-0.19}	0.09 ^{+0.01} _{-0.02}	—	—	—	—	—	1.10 (156)	—	—	—	—	—	—	—	—	—
	LN 0.62 ± 0.05	0.66 ± 0.05	—	—	—	—	—	—	—	—	—	—	—	—	—	—	—
AS1.04	2.059 ± 0.004	LC 0.0	0.0	—	—	—	—	—	—	—	—	—	—	—	—	14.82 ± 0.01	—
	LW 0.16 ± 0.02	1.89 ^{+0.25} _{-0.36}	—	—	—	—	—	—	1.07 (183)	—	—	—	—	—	—	—	—
	LN 1.98 ± 0.12	1.57 ± 0.09	—	—	—	—	—	—	—	—	—	—	—	—	—	—	—
NU1.05	1.771 ± 0.004	LC 0.0	0.0	0.0	—	—	—	—	—	—	—	—	—	—	—	47.55 ^{+0.81} _{-0.07}	—
	LW 3.42 ± 0.22	0.067 ^{+0.004} _{-0.005}	0.84 ^{+0.09} _{-0.08}	—	—	—	—	—	1.12 (137)	—	—	—	—	—	—	—	—
	LN 3.12 ± 0.15	5.79 ± 0.27	1.66 ± 0.19	—	—	—	—	—	—	—	—	—	—	—	—	—	—
NU1.06	1.879 ± 0.004	LC 0.0	0.0	—	—	—	—	—	—	—	—	—	—	—	—	24.92 ^{+0.08} _{-0.09}	—
	LW 4.24 ^{+0.43} _{-0.38}	0.54 ± 0.06	—	—	—	—	—	—	0.91 (99)	—	—	—	—	—	—	—	—
	LN 1.81 ± 0.10	1.79 ± 0.09	—	—	—	—	—	—	—	—	—	—	—	—	—	—	—
NU1.07	1.978 ± 0.003	LC 0.0	0.0	—	—	—	—	—	—	—	—	—	—	—	—	29.17 ^{+0.12} _{-0.10}	—
	LW 3.32 ^{+0.88} _{-0.67}	0.63 ± 0.10	—	—	—	—	—	—	1.04 (120)	—	—	—	—	—	—	—	—
	LN 0.37 ± 0.07	0.54 ± 0.05	—	—	—	—	—	—	—	—	—	—	—	—	—	—	—
NU1.08	1.95 ± 0.02	LC 0.0	—	—	—	—	—	—	—	—	—	—	—	—	—	26.21 ± 0.01	—
	LW 0.32 ^{+0.09} _{-0.10}	—	—	—	—	—	—	—	1.35 (161)	—	—	—	—	—	—	—	—
	LN 1.54 ± 0.26	—	—	—	—	—	—	—	—	—	—	—	—	—	—	—	—
NU1.09	1.90 ± 0.01	LC 0.0	0.0	0.0	—	—	—	—	—	—	—	—	—	—	—	38.28 ^{+0.11} _{-0.13}	—
	LW 2.78 ^{+0.78} _{-0.55}	0.21 ± 0.10	0.015 ^{+0.006} _{-0.004}	—	—	—	—	—	1.10 (224)	—	—	—	—	—	—	—	—
	LN 2.13 ± 0.19	1.25 ± 0.22	2.35 ± 0.68	—	—	—	—	—	—	—	—	—	—	—	—	—	—
AS1.10	2.012 ± 0.003	LC 0.0	0.0	—	—	—	—	—	—	—	—	—	—	—	—	15.220 ± 0.002	—
	LW 2.45 ^{+0.14} _{-0.15}	0.23 ± 0.02	—	—	—	—	—	—	0.99 (372)	—	—	—	—	—	—	—	—
	LN 4.24 ± 0.12	3.39 ± 0.15	—	—	—	—	—	—	—	—	—	—	—	—	—	—	—
NU1.11	1.48 ± 0.01	LC 0.0	—	—	—	—	—	—	—	—	—	—	—	—	—	1.64 ± 0.01	—
	LW 0.57 ^{+0.28} _{-0.30}	—	—	—	—	—	—	—	1.16 (164)	—	—	—	—	—	—	—	—
	LN 0.12 ± 0.07	—	—	—	—	—	—	—	—	—	—	—	—	—	—	—	—
NU1.12	1.907 ± 0.004	LC 0.0	—	—	—	—	—	—	—	—	—	—	—	—	—	1.50 ± 0.71	—
	LW 0.03 ^{+0.02} _{-1.07}	—	—	—	—	—	—	—	1.07 (181)	—	—	—	—	—	—	—	—
	LN 0.012 ± 0.008	—	—	—	—	—	—	—	—	—	—	—	—	—	—	—	—
NU1.13	1.920 ± 0.002	LC 0.0	—	—	—	—	—	—	—	—	—	—	—	—	—	2.89 ± 0.51	—
	LW 0.53 ± 0.22	—	—	—	—	—	—	—	1.05 (228)	—	—	—	—	—	—	—	—
	LN 0.04 ± 0.02	—	—	—	—	—	—	—	—	—	—	—	—	—	—	—	—
NU1.14	1.939 ± 0.004	LC 0.0	—	—	—	—	—	—	—	—	—	—	—	—	—	7.50 ± 0.03	—
	LW 9.48 ± 0.01	—	—	—	—	—	—	—	1.10 (392)	—	—	—	—	—	—	—	—
	LN 0.17 ± 0.08	—	—	—	—	—	—	—	—	—	—	—	—	—	—	—	—
NU1.15	1.938 ± 0.004	LC 0.0	0.0	—	—	—	—	—	—	—	—	—	—	—	—	19.04 ± 0.21	—
	LW 1.79 ^{+0.18} _{-0.15}	0.27 ± 0.03	—	—	—	—	—	—	1.07 (226)	—	—	—	—	—	—	—	—
	LN 0.76 ± 0.06	0.37 ± 0.03	—	—	—	—	—	—	—	—	—	—	—	—	—	—	—
NU1.16	1.928 ± 0.003	LC 0.0	0.0	0.0	—	—	—	—	—	—	—	—	—	—	—	35.63 ± 0.39	—
	LW 4.94 ^{+0.57} _{-0.67}	0.039 ^{+0.004} _{-0.003}	0.81 ± 0.10	—	—	—	—	—	1.18 (224)	—	—	—	—	—	—	—	—
	LN 1.03 ± 0.11	1.99 ^{+0.08} _{-0.07}	0.99 ± 0.07	—	—	—	—	—	—	—	—	—	—	—	—	—	—
NU1.17	1.970 ± 0.003	LC 0.0	0.0	0.0	—	—	—	—	—	—	—	—	—	—	—	23.52 ± 0.78	—
	LW 0.13 ± 0.01	3.75 ^{+1.20} _{-0.81}	0.0004 ± 0.0001	—	—	—	—	—	1.65 (272)	—	—	—	—	—	—	—	—
	LN 0.31 ± 0.02	0.27 ± 0.05	0.008 ± 0.003	—	—	—	—	—	—	—	—	—	—	—	—	—	—
AS1.18	1.998 ± 0.004	LC 0.0	0.0	0.0	—	—	—	—	—	—	—	—	—	—	—	26.67 ± 1.10	Type-C
	LW 4.97 ± 0.11	0.23 ± 0.01	0.03 ± 0.01	0.017 ± 0.004	0.03 ± 0.01	—	—	—	1.04 (499)	4.93	5.53 ± 0.32	—	—	—	—	—	—
	LN 17.28 ± 0.22	20.08 ± 0.65	2.98 ± 0.08	1.87 ± 0.36	1.16 ± 0.28	—	—	—	—	—	—	—	—	—	—	—	—
NU1.19	1.650 ± 0.004	LC 0.0	0.0	0.0	—	—	—	—	—	—	—	—	—	—	—	19.38 ± 1.08	Type-C
	LW 5.09 ^{+0.24} _{-0.23}	0.06 ± 0.01	0.26 ± 0.01	0.012 ^{+0.005} _{-0.004}	—	—	—	—	1.37 (223)	3.75	3.22 ± 0.37	—	—	—	—	—	—
	LN 0.75 ± 0.05	2.19 ± 0.30	0.21 ± 0.10	1.02 ^{+0.01} _{-0.22}	—	—	—	—	—	—	—	—	—	—	—	—	—
AS1.20	2.00 ± 0.01	LC 0.0	0.0	0.0	—	—	—	—	—	—	—	—	—	—	—	24.10 ± 0.55	Type-C
	LW 6.10 ± 0.15	0.14 ± 0.01	0.35 ± 0.02	0.03 ± 0.01	—	—	—	—	—	—	—	—	—	—	—	—	—
	LN 16.61 ± 0.26	9.21 ± 0.71	13.09 ± 3.31	1.52 ± 0.27	—	—	—	—	—	—	—	—	—	—	—	—	—
AS1.21	2.002 ± 0.006	LC 0.0	0.0	0.0	—	—	—	—	—	—	—	—	—	—	—	22.58 ± 0.23	—
	LW 6.56 ± 0.39	0.34 ± 0.05	0.16 ± 0.05	—	—	—	—	—	1.19 (372)	—	—	—	—	—	—	—	—
	LN 13.23 ± 0.24	6.36 ± 0.52	12.01 ± 0.95	—	—	—	—	—	—	—	—	—	—	—	—	—	—
AS1.22	2.02 ± 0.02	LC 0.0	0.0	0.0	—	—	—	—	—	—	—	—	—	—	—	22.28 ± 1.22	—
	LW 5.44 ^{+0.61} _{-0.53}	0.11 ^{+0.03} _{-0.04}	0.25 ± 0.04	—	—	—	—	—	0.97 (185)	—	—	—	—	—	—	—	—
	LN 13.79 ± 0.74	8.34 ± 1.64	11.07 ± 0.89	—	—	—	—	—	—	—	—	—	—	—	—	—	—
AS1.23	1.99 ± 0.02	LC 0.0	0.0	0.0	—	—	—	—	—	—	—	—	—	—	—	22.61 ± 0.60	—
	LW 7.18 ^{+0.90} _{-0.79}	0.38 ± 0.04	—														

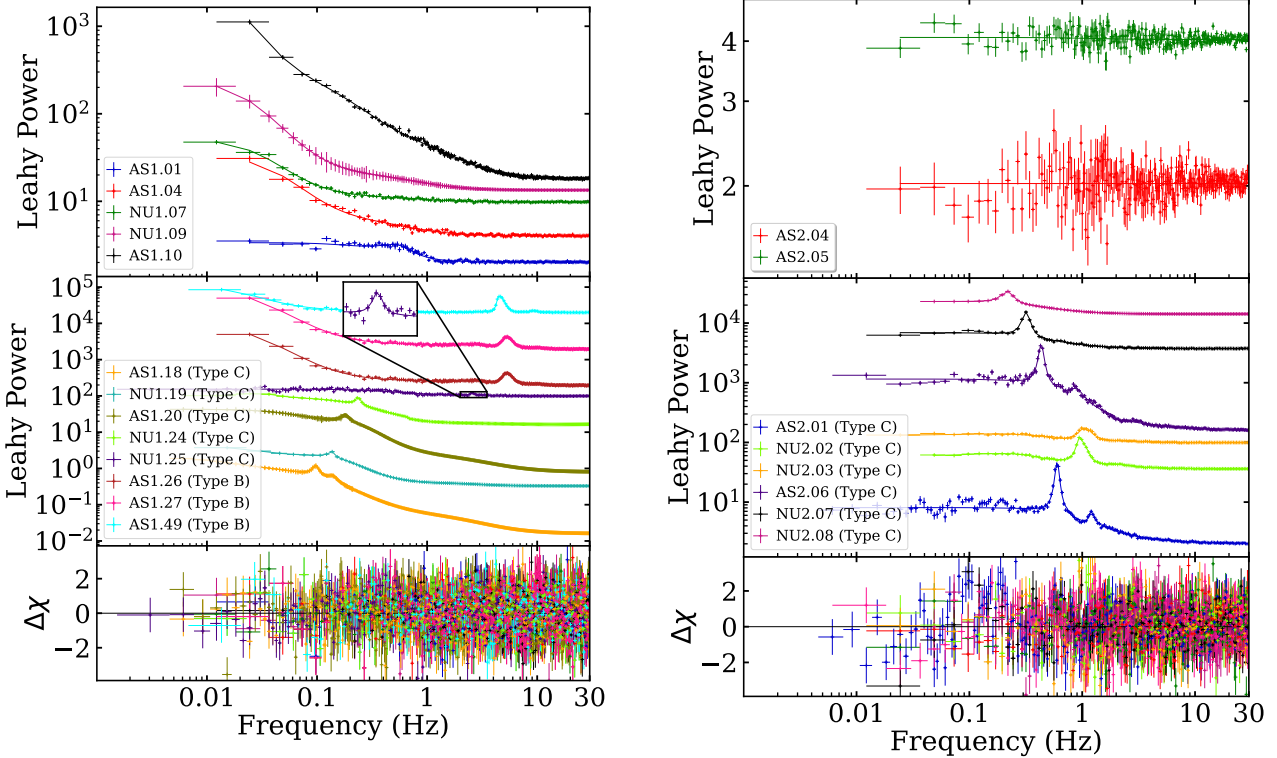


Figure 5. Power density spectra of GX 339–4 (left panel) and H 1743–322 (right panel) during different observations in the frequency range of 0.001 – 30 Hz. *Left panel:* PDS of GX 339–4 during quiescence – AS1.01 (blue), hard state – AS1.04 (red), NU1.07 (green), NU1.09 (magenta), AS1.10 (black), AS1.18 (orange), NU1.19 (sky blue), AS1.20 (olive), NU1.24 (lime), and intermediate state – NU1.25 (violet), AS1.26 (brown), AS1.27 (pink), AS1.49 (cyan) are shown. *Right panel:* PDS of H 1743–322 during quiescence – AS2.04 (red), AS2.05 (green) and hard state – AS2.01 (blue), NU2.02 (lime), NU2.03 (orange), AS2.06 (violet), NU2.07 (black) and NU2.08 (magenta). In both figures, bottom panels show residual variation of PDS fitting. The power corresponding to different epochs are scaled for the purpose of clarity. See the text for details.

PDS of other epochs of both sources in 0.001–30 Hz frequency range and present the model fitted parameters of power spectra in Table 4.

The detection of a QPO and its harmonic in the PDS of both sources prompted us to study the energy-dependent analysis of the power spectra. While doing so, we consider lightcurves in different energy bands and carry out the PDS analysis. For GX 339–4, we consider energy bands as 3 – 10 keV, 10 – 20 keV and 20 – 60 keV, whereas for H 1743–322, we choose 3 – 10 keV, 10 – 20 keV, 20 – 30 keV, 30 – 40 keV and 40 – 60 keV energy ranges. We extract model parameters from the best fit which are tabulated in Table 5. We also calculate the rms spectrum following the procedure described above.

5.1 GX 339–4

It is observed that for GX 339–4, QPO frequency increases with the decrease of total PDS power during 2021 outburst. Moreover, the source renders total variability as 2.82–26.25% rms, 14.82–59.36% rms, 1.22–47.10% rms and 0.75–2.63% rms in quiescent, hard, intermediate and soft states respectively. During seven epochs (AS1.18, NU1.19, AS1.20, NU1.24, NU1.25, AS1.26 and AS1.27) in the 2021 outburst, GX 339–4 exhibits QPO features, where fundamental QPO frequency (ν_{QPO}) varies in the range 0.097 – 5.37 Hz with significance (σ) as 3.3 – 21.96 and $\text{QPO}_{\text{rms}}\%$ as 2.08 – 5.53. In addition, we find that ν_{QPO} increases monotonically as time progresses which is shown in the middle panel of Fig. 5 (left panel). A rapid evolution is observed between epoch AS1.26 to AS1.27 (separated by only

a day), where ν_{QPO} evolves from 5.37 ± 0.02 Hz to $4.85^{+0.01}_{-0.02}$ Hz. During epoch AS1.26, GX 339-4 shows sub-harmonic and second harmonic around 2.86 Hz and 9.83 Hz, respectively. Interestingly, in epoch AS1.27, the sub-harmonic disappears and second harmonic is seen at ~ 9.78 Hz. The results of similar kind are also reported in the literature (Mondal et al. 2023; Peirano et al. 2023). Recently, GX 339-4 has shown QPOs during three epochs (NU1.46, NU1.48 and AS1.49) of 2023 – 2024 outburst with ν_{QPO} varies in the range 0.46 – 4.49 Hz with σ in the range 2.10 – 8.41 and $\text{QPO}_{\text{rms}}\%$ as 3.68 – 9.97. We observe second harmonic during AS1.49 around 9.32 Hz. We classify QPOs belonging to AS1.18, NU1.19, AS1.20, NU1.24, NU1.25, NU1.46 as type-C, and those in AS1.26, AS1.27, NU1.48, AS1.49 as type-B (see Motta et al. 2011, for details). Needless to mention that the observed QPOs are associated with either LHS or IMS.

In Table 5, we present the energy dependent model fitted parameters for each epochs where QPO is present. In all epochs, we find that QPO feature disappears in 20 – 60 keV energy band. Moreover, we do not find any significant detection of QPO after 10 keV for epoch AS1.20 and epoch NU1.25. During epoch AS1.26, ν_{QPO} and its sub-harmonic are absent beyond 20 keV, and the second harmonic is seen in 3 – 10 keV energy range. On the other hand, we notice that during epoch AS1.27, the second harmonic is present only in 3 – 10 keV range and the QPO signature disappears above 20 keV, as shown in Fig. 6.

Table 5. Energy-dependent QPO parameters of GX 339–4 and H 1743–322 from *NuSTAR* and *LAXPC* observations in the period 2016–2024. Power spectra have been modeled in Leahy space. The parameters corresponding to the fundamental component are indicated with f, sub-harmonic with sub and second harmonic as I^{st} .

Epoch	E-band keV	QPO (f) Hz	FWHM (f) Hz	Norm (f)	Q (f)	sig (f)	rms (f) (per cent)	QPO (sub) Hz	FWHM (sub) Hz	Norm (sub)	Q (sub)	sig (sub)	rms (sub) (per cent)	QPO (I^{st}) Hz	FWHM (I^{st}) Hz	Norm (I^{st})	Q (I^{st})	sig (I^{st})	rms (I^{st}) (per cent)	
GX 339–4																				
AS1.18	3–10	0.097 ± 0.004	0.00105 ± 0.00008	0.08 ± 0.03	8.32	2.66	25.39 ± 0.02	—	—	—	—	—	—	—	—	—	—	—	—	
	10–20	0.09 ± 0.01	0.0013 ± 0.0006	0.02 ± 0.01	7.39	2.00	23.61 ± 0.20	—	—	—	—	—	—	—	—	—	—	—	—	
	20–60	—	—	—	—	—	—	—	—	—	—	—	—	—	—	—	—	—	—	
NU1.19	3–10	0.133 ± 0.002	0.007 ^{+0.003} _{-0.001}	0.15 ± 0.04	16.34	4.08	18.73 ± 0.21	—	—	—	—	—	—	—	—	—	—	—	—	
	10–20	0.14 ± 0.01	0.08 ± 0.01	0.22 ± 0.03	1.80	7.58	18.05 ± 0.22	—	—	—	—	—	—	—	—	—	—	—	—	
	20–60	—	—	—	—	—	—	—	—	—	—	—	—	—	—	—	—	—	—	
AS1.20	3–10	0.18 ± 0.02	0.011 ^{+0.003} _{-0.001}	0.50 ± 0.34	16.22	1.46	3.24 ± 0.21	—	—	—	—	—	—	—	—	—	—	—	—	
	10–20	—	—	—	—	—	—	—	—	—	—	—	—	—	—	—	—	—	—	
	20–60	—	—	—	—	—	—	—	—	—	—	—	—	—	—	—	—	—	—	
NU1.24	3–10	0.231 ± 0.003	0.02 ± 0.01	0.11 ± 0.03	11.92	3.51	17.64 ± 0.17	—	—	—	—	—	—	—	—	—	—	—	—	
	10–20	0.242 ± 0.001	0.070 ^{+0.020} _{-0.020}	0.11 ^{+0.05} _{-0.02}	3.45	5.35	16.88 ± 0.76	—	—	—	—	—	—	—	—	—	—	—	—	
	20–60	—	—	—	—	—	—	—	—	—	—	—	—	—	—	—	—	—	—	
NU1.25	3–10	2.62 ^{+0.04} _{-0.03}	0.33 ^{+0.17} _{-0.11}	0.40 ^{+0.03} _{-0.04}	7.79	7.01	14.79 ± 0.56	—	—	—	—	—	—	—	—	—	—	—	—	
	10–20	—	—	—	—	—	—	—	—	—	—	—	—	—	—	—	—	—	—	
	20–60	—	—	—	—	—	—	—	—	—	—	—	—	—	—	—	—	—	—	
AS1.26	3–10	5.249 ± 0.004	1.13 ± 0.25	3.96 ± 0.38	4.64	10.42	7.20 ± 0.25	2.66 ± 0.16	1.32 ± 0.36	0.81 ± 0.17	2.01	4.76	3.25 ± 0.45	10.86 ^{+0.38} _{-0.76}	1.17 ± 0.82	0.28 ± 0.15	9.28	1.87	1.92 ± 0.35	
	10–20	5.56 ± 0.16	0.88 ^{+0.32} _{-0.57}	0.43 ^{+0.15} _{-0.13}	6.32	3.31	7.15 ± 0.77	3.04 ± 0.19	0.33 ± 0.22	0.11 ± 0.06	9.21	1.83	3.61 ± 0.62	—	—	—	—	—	—	
	20–60	—	—	—	—	—	—	—	—	—	—	—	—	—	—	—	—	—	—	
AS1.27	3–10	4.89 ± 0.02	0.50 ^{+0.03} _{-0.02}	4.24 ± 0.16	9.78	7.56	7.56 ± 0.06	—	—	—	—	—	—	—	9.76 ± 0.20	1.38 ± 0.38	0.55 ± 0.12	7.07	4.58	2.72 ± 0.65
	10–20	4.81 ± 0.04	0.52 ^{+0.10} _{-0.09}	0.73 ± 0.09	9.25	8.11	9.78 ± 0.16	—	—	—	—	—	—	—	—	—	—	—	—	
	20–60	—	—	—	—	—	—	—	—	—	—	—	—	—	—	—	—	—	—	
NU1.46	3–10	0.463 ± 0.002	0.07 ± 0.02	0.38 ± 0.10	6.61	3.8	4.56 ± 0.20	—	—	—	—	—	—	—	—	—	—	—	—	
	10–20	0.463 ± 0.004	0.06 ± 0.01	0.07 ± 0.01	7.75	7.0	1.89 ± 0.02	—	—	—	—	—	—	—	—	—	—	—	—	
	20–60	—	—	—	—	—	—	—	—	—	—	—	—	—	—	—	—	—	—	
NU1.48	3–10	4.52 ± 0.03	0.38 ± 0.11	0.21 ± 0.09	11.89	2.33	3.49 ± 0.12	—	—	—	—	—	—	—	—	—	—	—	—	
	10–20	4.59 ± 0.12	0.68 ± 0.12	0.13 ^{+0.03} _{-0.04}	6.74	3.25	2.56 ± 0.12	—	—	—	—	—	—	—	—	—	—	—	—	
	20–60	—	—	—	—	—	—	—	—	—	—	—	—	—	—	—	—	—	—	
AS1.49	3–10	4.50 ± 0.01	0.27 ± 0.03	1.09 ± 0.19	16.66	5.73	7.33 ± 0.32	—	—	—	—	—	—	—	9.26 ± 0.07	1.47 ^{+0.41} _{-0.33}	0.41 ± 0.07	6.27	5.85	4.49 ± 0.42
	10–20	4.67 ± 0.02	0.66 ± 0.05	0.55 ^{+0.05} _{-0.07}	7.00	7.86	5.16 ± 0.23	—	—	—	—	—	—	—	9.51 ^{+0.69} _{-0.41}	1.36 ± 0.72	0.12 ± 0.06	6.99	1.89	2.41 ± 0.12
	20–60	—	—	—	—	—	—	—	—	—	—	—	—	—	—	—	—	—	—	
H 1743–322																				
AS2.01	3–10	0.599 ± 0.003	0.058 ± 0.004	2.79 ± 0.16	10.32	17.43	13.31 ± 0.08	—	—	—	—	—	—	—	1.22 ± 0.01	0.14 ^{+0.06} _{-0.04}	0.51 ± 0.06	8.71	8.50	5.69 ± 0.47
	10–20	0.602 ± 0.003	0.068 ± 0.006	1.21 ± 0.08	8.85	15.13	13.51 ± 0.09	—	—	—	—	—	—	—	1.22 ± 0.02	0.16 ^{+0.11} _{-0.07}	0.19 ^{+0.09} _{-0.06}	7.63	3.17	5.35 ± 0.56
	20–30	0.602 ± 0.007	0.08 ± 0.02	0.19 ^{+0.04} _{-0.03}	7.53	6.33	16.79 ± 0.96	—	—	—	—	—	—	—	—	—	—	—	—	—
NU2.02	3–10	0.981 ± 0.006	0.20 ^{+0.03} _{-0.01}	0.86 ± 0.02	4.78	43.38	16.68 ± 0.10	—	—	—	—	—	—	—	—	—	—	—	—	—
	10–20	0.97 ± 0.01	0.22 ± 0.04	0.48 ± 0.03	4.49	23.96	35.72 ± 0.28	—	—	—	—	—	—	—	—	—	—	—	—	—
	20–30	0.95 ± 0.03	0.19 ^{+0.11} _{-0.07}	0.05 ± 0.02	5.00	2.78	14.50 ± 0.44	—	—	—	—	—	—	—	—	—	—	—	—	—
NU2.03	30–40	—	—	—	—	—	—	—	—	—	—	—	—	—	—	—	—	—	—	—
	40–60	—	—	—	—	—	—	—	—	—	—	—	—	—	—	—	—	—	—	—
	3–10	1.07 ± 0.01	0.23 ^{+0.03} _{-0.02}	0.51 ± 0.02	4.60	25.57	16.68 ± 0.10	—	—	—	—	—	—	—	—	—	—	—	—	—
AS2.06	10–20	1.09 ± 0.01	0.42 ± 0.03	0.34 ± 0.02	2.53	18.87	14.02 ± 0.21	—	—	—	—	—	—	—	—	—	—	—	—	—
	20–30	1.08 ± 0.05	0.31 ± 0.11	0.05 ± 0.01	3.48	5.00	12.55 ± 0.45	—	—	—	—	—	—	—	—	—	—	—	—	—
	30–40	—	—	—	—	—	—	—	—	—	—	—	—	—	—	—	—	—	—	—
AS2.07	40–60	—	—	—	—	—	—	—	—	—	—	—	—	—	—	—	—	—	—	—
	3–10	0.317 ± 0.002	0.06 ± 0.01	1.11 ± 0.04	5.79	27.87	35.15 ± 0.13	—	—	—	—	—	—	—	—	—	—	—	—	—
	10–20	0.32 ± 0.01	0.05 ^{+0.02} _{-0.01}	0.28 ± 0.03	6.29	9.95	23.37 ± 0.31	—	—	—	—	—	—	—	—	—	—	—	—	—
NU2.08	20–30	0.32 ± 0.01	0.04 ± 0.02	0.03 ± 0.01	7.64	3.66	17.00 ± 0.42	—	—	—	—	—	—	—	—	—	—	—	—	—
	30–40	—	—	—	—	—	—	—	—	—	—	—	—	—	—	—	—	—	—	—
	40–60	—	—	—	—	—	—	—	—	—	—	—	—	—	—	—	—	—	—	—

5.2 H 1743–322

In Fig. 5 (right panel), we present the PDS for selected epochs. In particular, we find QPO features during six epochs, namely AS2.01, NU2.02, NU2.03, AS2.06, NU2.07 and NU2.08, respectively, where the fundamental QPO frequency (ν_{QPO}) varies in the range 0.22–1.03 Hz with significance (σ) as 8.31–19.74 and QPO_{rms}% as 7.31–12.21. What is more is that we observe the presence of fundamental QPO (ν_{QPO}) along with its harmonic during three epochs. For epochs AS2.01, AS 2.06 and NU2.07, ν_{QPO} and its harmonic are estimated as 0.6 Hz and 1.20 Hz, 0.43 Hz and 0.87 Hz, and 0.32 Hz and 0.66 Hz, respectively. We observe that H 1743–322 shows total variability of 1.41–2.16% rms and 18.81–46.23% rms during the quiescent and hard states. Further, we carry out the energy dependent analysis of PDS and depict the obtained results in Fig. 7. We find that QPO feature continues to present in the energy range 3–40 keV for the epochs AS2.01 and AS2.06, whereas harmonics disappears for energy beyond 20 keV. For the remaining epochs, QPO is seen in 3–30 keV energy range only. All the model extracted parameters are tabulated in Table 5.

6 DISCUSSIONS AND CONCLUSIONS

In this work, we present the comprehensive analyses of wide-band spectro-temporal variabilities of two BH-XRBs, namely GX 339–4 and H 1743–322, using *AstroSat* and *NuSTAR* observations during 2016–2024. Since their discovery, it was observed that both sources underwent frequent outbursts (Homan et al. 2005b; Belloni et al. 2005; Tomsick et al. 2008; Del Santo et al. 2009; Shaposhnikov & Titarchuk 2009; Capitanio et al. 2010; Debnath et al. 2010; Chen et al. 2010; Debnath et al. 2013; Nandi et al. 2012; Sreehari et al. 2018, 2019a). In particular, during the observation period of our interest, H 1743–322 and GX 339–4 exhibited four and six outbursts, respectively, followed by the long term evolution as shown in Fig. 2. Meanwhile, Aneesha et al. (2019); Aneesha & Mandal (2020); Bhowmick et al. (2021) examined the outburst triggering mechanism in these sources. These authors indicated that during quiescence phase, matter accumulates inside the disc and slowly diffuses inwards. Accordingly, the disc mass builds up until at some disc radius where the local accretion rate increases above its critical limit. It is believed that, the sudden rise of viscosity due to the increase in accretion rate can lead to the triggering of outburst in BH-XRBs (Ebisawa et al.

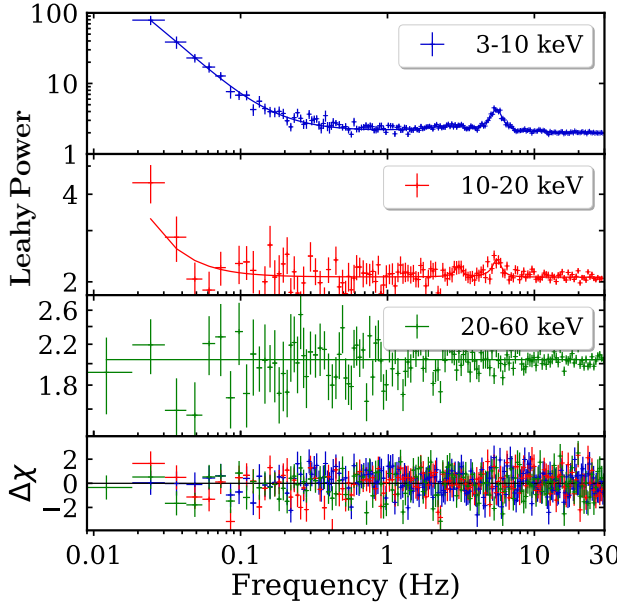


Figure 6. Energy-dependent PDS (LAXPC) of GX 339–4 in Leahy space during epoch AS1.26 (MJD 59303.06). PDS are shown in the energy range 3 – 10 keV (blue), 10 – 20 keV (red) and 20 – 60 keV (green) starting from top panel, respectively. The residual variation is presented in the bottom panel. See the text for details.

1996; Lasota 2001; Seifina & Titarchuk 2010; Seifina et al. 2014; Titarchuk & Seifina 2017, 2021).

After triggering of the outburst, the outer part of the disc becomes hot due to the strong irradiation originated from the inner disc (van Paradijs 1996; King & Ritter 1998; Shahbaz et al. 1998). Because of this, viscosity is enhanced that allows the Keplerian disc to move towards the central BH (Chakrabarti 1990). Since the supply of soft photons is increased, more and more seed photons are up-scattered leading the accreting system to transit towards the soft state via intermediate states. As time evolves, disc starts getting depleted due to the reduction of matter supply from the companion (Hameury et al. 1986; Hameury & Lasota 2014) and hence, the temperature of the disc is decreased. At this point, outburst declines and possibly, source transits towards the quiescent accretion phase.

Both GX 339–4 and H 1743–322 experienced *successful* as well as *failed* outbursts during 2016 – 2024 (see §3). The 2019 – 2020, 2021 and 2023 – 2024 outbursts of GX 339–4 appeared as *successful* one that shows canonical HID patterns (left panel of Fig. 3; see also Sreehari et al. 2018; Nandi et al. 2018; Baby et al. 2021; Dong et al. 2021; Prabhakar et al. 2022; Wang et al. 2022b) and also exhibited longer duration with slow rise slow decay profile. These two outbursts are the brightest and they perhaps occurred due to the high mass accretion rate ($L_{\text{bol}} \gtrsim 19.59\% L_{\text{Edd}}$, see Table 3). On the contrary, during 2017 – 2018 and 2018 – 2019, GX 339–4 underwent *failed* outburst (Husain et al. 2022; Debnath et al. 2023) yielding low luminosity possibly resulted due to the lack of matter supply from the companion. According to Wang et al. (2022a), *failed* and *successful* outbursts follow the same initial evolutionary track, although the former class of outburst never reaches the threshold for a transition to thermally dominated accretion regimes. It is interesting to note that for 2018 – 2019, 2019 – 2000, 2021 and 2023 – 2024 outbursts, the rising time in 2 – 6 keV energy band is longer than the same in 6 – 20 keV energy band (see Table 2). Fig. 2a shows that the soft (2 – 20 keV) lightcurve lags behind hard (15 – 50 keV)

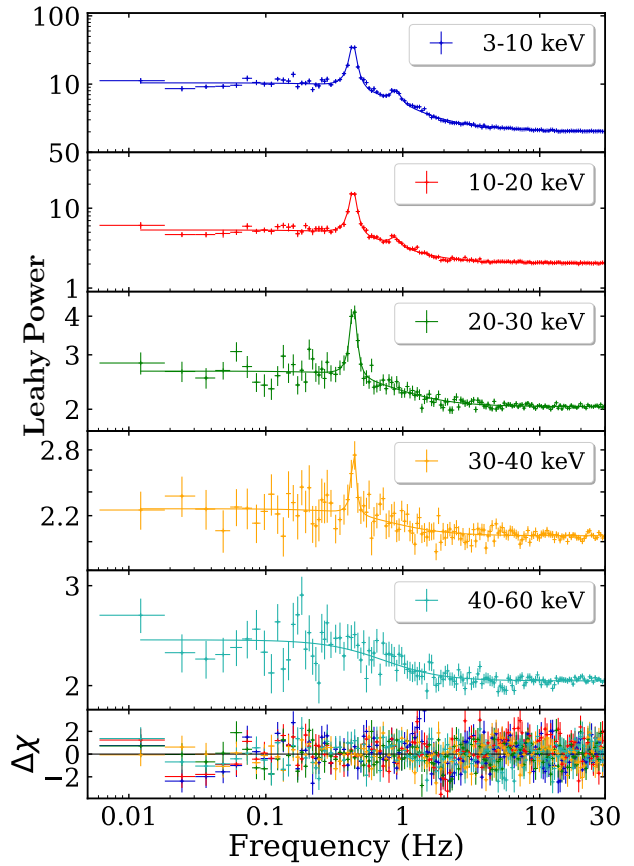


Figure 7. Energy-dependent PDS (LAXPC) of H 1743–322 in Leahy space during epoch AS2.06 (MJD 57973.32). PDS are shown in the energy range 3 – 10 keV (blue), 10 – 20 keV (red), 20 – 30 keV (green), 30 – 40 keV (orange) and 40 – 60 keV (sky blue) starting from top panel, respectively. The residual variation is presented in the bottom panel. See the text for details.

lightcurve during 2019 – 2020, 2021 and 2023 – 2024 outbursts. The fast rise and fast decay of hard photon counts unlike the soft photon counts indicates the presence of two distinct components of accretion flow comprising Keplerian and sub-Keplerian matters (Chakrabarti & Titarchuk 1995) which accrete at two different time scales (Aneesha et al. 2019; Aneesha & Mandal 2020). Furthermore, H 1743–322 underwent four outbursts. Among them only 2016a outburst was successful (Stiele & Kong 2021b) although all four outbursts yield similar luminosity with shorter duration. Here, we infer that during the previous outburst, a part of the disc matter may not be fully accreted by the central BH. Eventually, the left over mass can combine with the material accreted from the companion star and ultimately contributes in triggering the 2016a outburst (Chakrabarti et al. 2019).

We observe that both GX 339–4 and H 1743–322 passed through quiescence phases multiple times during the observation period under consideration. The quiescence state spectra of GX 339–4 and H 1743–322 sources are satisfactorily described by the non-thermal Comptonization model (Nthcomp). We find that photon index (Γ_{nth}) varies as 1.71 – 2.48 and 1.56 – 2.22 for GX 339–4 and H 1743–322, respectively, which are in accordance with the usual quiescent spectral indices of BH-XRBs (Kong et al. 2000; Corbel et al. 2006; Bradley et al. 2007; Plotkin et al. 2013). The luminosity of GX 339–4 and H 1743–322 are obtained as 0.03 – 0.06% L_{Edd} and 0.10 – 0.16% L_{Edd} . These luminosities are generally higher compared

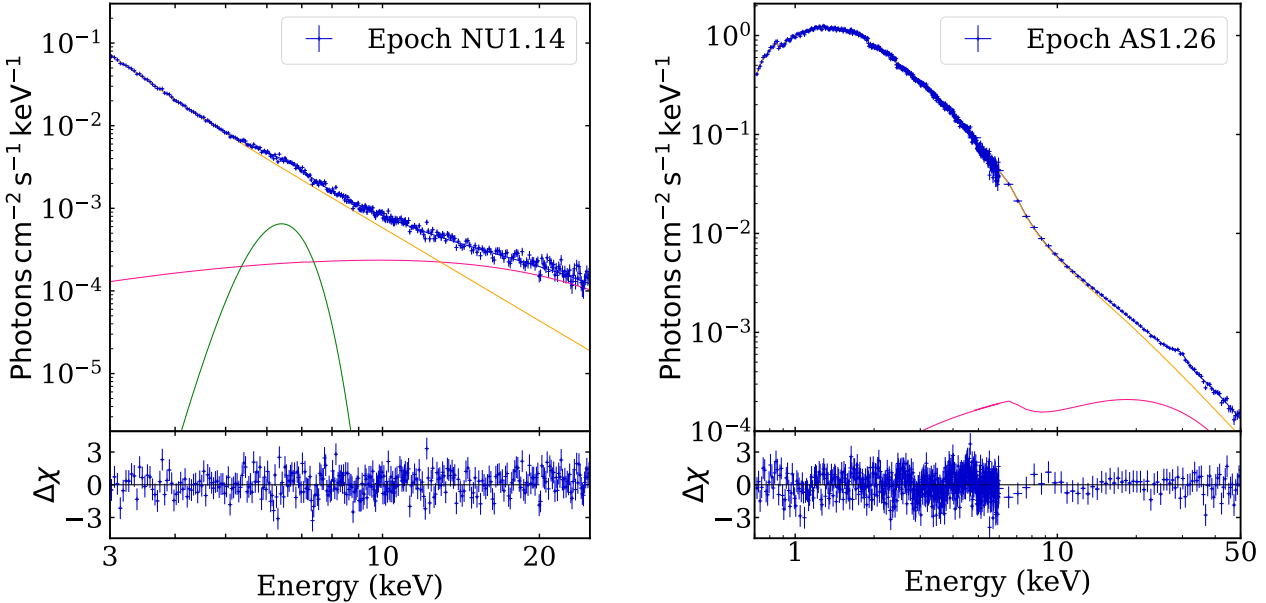


Figure 8. Energy spectra of GX 339–4 including annihilation lines (modelled with `bbody`) corresponding to epoch NU1.14 (left panel) and epoch AS1.26 (right panel) are modelled using `TBabs`×(`bbody+gaussian+comptb`) with $\chi^2_{\text{red}} = 0.97$ (543 dof) and `TBabs`×`smedge`×(`bbody+comptb`) with $\chi^2_{\text{red}} = 1.21$ (592 dof), respectively. Unfolded model components of `bbody`, `comptb` and `gaussian` are depicted by pink, orange and green solid curves, whereas plus signs represent observational data. See the text for the details.

to the quiescence state luminosity of other BH-XRBs (Remillard et al. 2006). Similarly, to explain the hard state spectra of GX 339–4 and H 1743–322, we model the source spectra using `Nthcomp` model component. In the hard state of GX 339–4, we obtain $\Gamma = 1.54 - 1.74$, $kT_{\text{bb}} \sim 0.12 - 0.77$ keV and $kT_{\text{e}} \sim 4.33 - 106.82$ keV, which are in good agreement with the previous findings (Dzielak et al. 2019; Wang-Ji et al. 2018). In the case of H 1743–322, in the hard state $\Gamma_{\text{nth}} \sim 1.57 - 1.71$ and $kT_{\text{e}} \sim 17.37 - 50.0$ keV which is in accordance with Dong et al. (2021). The corresponding luminosities for GX 339–4 and H 1743–322 are estimated as 0.91 – 11.56 % L_{Edd} and 2.08 – 3.48 % L_{Edd} which are in good agreement with the observed luminosity of other BH-XRBs in hard states (Maccarone 2003). In explaining the intermediate states of GX 339–4, an additional thermal disc component (`diskbb`) is required along with the `Nthcomp` component. Best fit model yields the inner disc temperature as $kT_{\text{in}} \sim 0.56 - 0.88$ keV, $\Gamma_{\text{nth}} \sim 1.76 - 2.66$ and $kT_{\text{e}} \sim 11.43 - 50.00$ keV which agree with the results reported earlier (Shaposhnikov & Titarchuk 2009; Sridhar et al. 2020). The higher kT_{in} suggests that inner disc extends further towards BH. When GX 339–4 transits to softer state, the photon index becomes steeper $\Gamma_{\text{nth}} \sim 1.46 - 3.26$, disc becomes hotter as $kT_{\text{in}} \sim 0.82 - 0.88$ keV, and electron temperature decreases as $kT_{\text{e}} \sim 1.63 - 32.36$ keV (Plant et al. 2014; Liu et al. 2022). Moreover, we find maximum bolometric luminosity as $L_{\text{bol}} \sim 30.06\% L_{\text{Edd}}$ (2019 – 2020 outburst) that possibly indicates the presence of thermally dominated disc. Additionally, we also examine the High-temperature Blackbody Bump (HBB) features in IMS spectra of *AstroSat* and *NuSTAR* observations. Towards this, we model *NuSTAR* spectrum (epoch NU1.14) using model `TBabs`×(`comptb+gaussian+bbody`) and *AstroSat* spectrum (epoch AS1.26) using model `TBabs`×`smedge`(`comptb+bbody`). We find `bbody` colour temperature varies at $\sim 4 - 6$ keV in the IMS spectra. In Fig. 8, we plot the energy spectra including the annihilation lines (modelled with `bbody`) for epoch NU1.14 (left panel) and AS1.26 (right panel), respectively for GX 339–4 source. This possibly indicates the presence of weak signature of gravitationally

redshifted annihilation line as argued by Titarchuk & Seifina (2009); Seifina & Titarchuk (2010); Titarchuk & Seifina (2021).

In Fig. 9, we plot the variation of photon index Γ_{nth} with electron temperature kT_{e} for GX 339–4 (left panel) and H 1743–322 (right panel). In both panels, open triangles represent results when kT_{e} is kept frozen to obtain the best fit, while open circles denote results obtained without such restriction. We observe that for GX 339–4, Γ_{nth} lies in the range $\sim 1.5 - 3.25$ for $kT_{\text{e}} \sim 10$ keV. We also find that Γ_{nth} generally decreases with the increase of kT_{e} , although few exceptions are observed. For H 1743–322, we observe Γ_{nth} ranging approximately $\sim 1.55 - 2.2$, with any significant variation with electron temperatures kT_{e} below 50 keV, as the source predominantly remains in LHS. Meanwhile, using Monte Carlo simulations, Laurent & Titarchuk (2011) revealed a negative correlation between Γ_{nth} and kT_{e} . In addition, Seifina et al. (2014) reported similar variation of Γ_{nth} with kT_{e} for 4U 1630–47 source. These findings clearly indicates that as BH-XRBs transit from LHS to HSS, the corona cools down as it interacts with soft photons emitted from the accretion disc.

During the 2021 outburst, the hard state of GX 339–4 was completely characterized by Comptonize emissions without any signature of disc component. As outburst progresses, the signature of disc component gradually emerges out with the increase of `Nthcomp` flux. This happens as more and more disc photons are up-scattered by the corona via Comptonization. In this spectral state, we observe type-C QPO and as time evolves, QPO frequency increases in epoch AS1.18, NU1.19 and AS1.20, respectively that evidently indicates that the overall size of the corona decreases (Nandi et al. 2012). The evolution of the QPO frequency along the outburst is commonly observed in BH-XRB sources (Motta et al. 2011; Zhang et al. 2017). After epoch AS1.20 (*i.e.*, during epochs AS1.21, AS1.22, AS1.23), the `Nthcomp` flux decreases and we see that the QPO features also disappears. As the source moves to hard peak (epoch NU1.24: hard peak is the peak during 2021 outburst in Fig. 2 (purple curve)), the `Nthcomp` flux increases and type-C QPO reappears. This possibly indicates that QPO feature seems to be an observable provided `Nthcomp` flux is suffi-

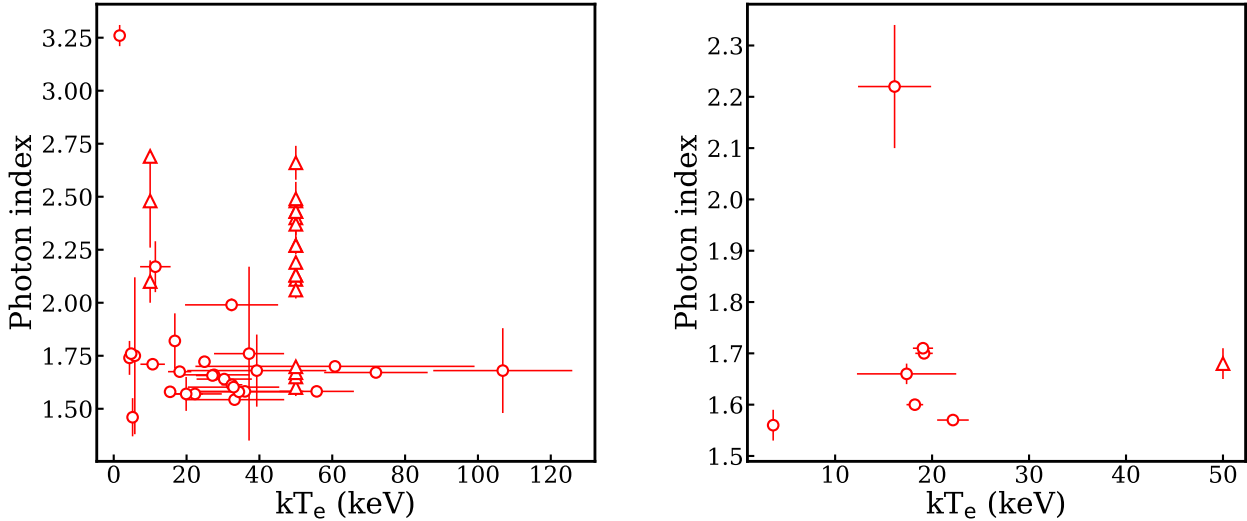


Figure 9. Variation of photon index Γ_{nth} with kT_e for GX 339–4 (left) and H 1743–322 (right). Open triangle corresponds to the results for frozen kT_e , and open circles denote results when such restriction is not imposed. See the text for the details.

ciently high. After the hard peak, the disc flux contribution increases which indicates that accretion disc evolves and the source transits to intermediate state (epoch NU1.25). After epoch NU1.25, the source transits to disc dominated intermediate state ($F_{\text{diskbb}} > F_{\text{nth}}$) and we observe type-B QPO along with sub-harmonic and second harmonic features in the PDS during epoch AS1.26 and AS1.27. Notably, the type-C QPO is observed along with flat-top noise, while red noise accompanies the type-B QPO. Subsequently, the Nthcomp flux starts decreasing and ultimately, QPO disappears in epoch AS1.28. At the peak of the outburst, the disc flux increases and source transits to soft state (epoch AS1.34). We find that the source continues to stay in the soft state (\sim MJD 59400) until it starts declining from peak the outburst (see Fig. 2). Similarly, we observe type-C QPO during two *AstroSat* and four *NuSTAR* observations of H 1743–322 which belong to 2016a, 2017 and 2018 outbursts where 2016a was successful outburst. The source was in hard state (see also Debnath et al. 2013) and the centroid QPO frequency varies as 0.22 – 1.01 Hz. As outburst progresses, QPO frequency is increased and the source spectra becomes softer which suggests the overall decrease of corona size. We see the presence of type-C QPO when F_{nth} value is high. It apparently suggests that the modulation of corona (Molteni et al. 1996; Das et al. 2014) possibly be responsible for the origin of type-C QPO in H 1743–322. We notice the presence of QPO in H 1743–322 irrespective to *successful* or *failed* outburst, whereas type-B and type-C QPOs are only seen during the *successful* outburst in GX 339–4. Recently, Lucchini et al. (2023) indicated that the source variability systematically evolves few days ahead of the canonical state transition, which is eventually quantified due to the change in spectral hardness during a successful outburst. Interestingly, the evolution of such kind of variability is not seen during the failed outburst, and hence, it possibly be regarded as the predictor to recognise a given outburst as *failed* or *successful* one. Needless to mention that any further investigation towards this is beyond the scope of the present paper due to the lack of pointed observation during the failed as well as successful outbursts.

It may be noted that in order to explain the origin of type-C QPOs, several models were proposed in the literature, namely relativistic precession model (RPM; Stella & Vietri 1998; Stella et al. 1999), precession of hot-inner flow model (Ingram et al. 2009), and prop-

agating oscillatory shock model (POS; Chakrabarti et al. 2008; Iyer et al. 2015). However, the origin of type-B QPO is not well understood as it was indicated that type-B QPO may be resulted due to the instabilities (Titarchuk & Osherovich 1999; Tagger & Pellat 1999) or possibly be associated with the disc-jet coupling mechanism (Fender et al. 2009; Radhika & Nandi 2014; Radhika et al. 2016; Kylafis et al. 2020), and hence, it remains inconclusive till date.

Meanwhile, it is reported that QPO frequency seems to be inversely proportional to the truncation radius of the disc (Chakrabarti & Manickam 2000; Titarchuk & Osherovich 2000). As the source transits from LHS to IMS, the truncation radius moves inward resulting the increase of QPO frequency as observed during 2021 outburst of GX 339–4, where QPO frequency monotonically increases from 0.10 Hz to 5.37 Hz. Indeed, the evolution of QPO frequency during an outburst was observed earlier in GX 339–4 (Nandi et al. 2012) and such features are commonly observed in other BH-XRBs (Motta et al. 2011; Zhang et al. 2017). Furthermore, QPOs are not generally observed in HSS of BH-XRBs (Belloni 2005; Nandi et al. 2012; Radhika et al. 2016), and similarly, we do not find QPOs in HSS of GX 339–4.

Furthermore, the energy dependent PDS analyses show that for GX 339–4, the fundamental QPO and its harmonics (if exist) are present in 3–20 keV. On the contrary, for H 1743–322, the fundamental QPO is only visible in 3–40 keV and harmonics disappear beyond 20 keV. We examine the energy dependent $\text{QPO}_{\text{rms}}\%$ spectra for GX 339–4 and H 1743–322. We observe that for both sources, $\text{QPO}_{\text{rms}}\%$ for type-C QPO is decreased with energy, whereas marginal changes are seen for type-B QPO (see Table 5). We also notice that when type-B QPO is observed, the corona size is reduced due to the effect of disc thermal emission. Because of this, the inner disc temperature is increased resulting in higher rms amplitude of QPO at high energies. This finding are in agreement with the results reported by Kong et al. (2020); Kara et al. (2019).

Based on the above findings, we summarize our results below.

- During the observation period of 2016 – 2024, H 1743–322 and GX 339–4 underwent four and six outbursts, respectively. The overall profile of the outbursts shows that GX 339–4 exhibits short rise slow decay, while H 1743–322 displays fast rise slow decay.
- The HID shows hysteresis pattern during 2019 – 2020, 2021

and 2023 – 2024 successful outbursts of GX 339–4, whereas the same is not observed during the successful outburst of H 1743–322 in 2016a.

- GX 339–4 is found to transit from quiescence ($L_{\text{bol}} = 0.03 - 0.06 \%\text{L}_{\text{Edd}}$) to outburst phase and vice versa. During outburst, the source exhibits hard, intermediate and soft spectral states with L_{bol} of $0.91 - 11.56 \%\text{L}_{\text{Edd}}$, $2.90 - 16.09 \%\text{L}_{\text{Edd}}$ and $19.59 - 30.06 \%\text{L}_{\text{Edd}}$, respectively. The quiescent state and hard state spectra are modelled with Comptonization component alone. Intermediate and soft state spectra require strong disc component along with weaker ‘Comptonization’ component.
- H 1743–322 is found to transit from quiescence ($L_{\text{bol}} \sim 0.10 - 0.16 \%\text{L}_{\text{Edd}}$) to hard state ($2.08 - 3.48 \%\text{L}_{\text{Edd}}$). The source does not show any thermal disc component in its energy spectrum.
- Both type-B and type-C QPO signatures in the frequency range $0.10 - 5.37$ Hz are observed in GX 339–4. In particular, type-C QPOs in both hard and intermediate states are observed where corona emission is dominant ($F_{\text{nth}} > F_{\text{diskbb}}$), whereas type-B QPO is observed for $F_{\text{diskbb}} > F_{\text{nth}}$. On the contrary, only type-C QPO is found in the hard state of H 1743–322 with frequencies in the range $0.22 - 1.01$ Hz. Note that both sources exhibit QPO harmonics.
- The energy dependent PDS study shows that in GX 339–4, the fundamental QPO and harmonics disappear beyond 20 keV. In H 1743–322, the fundamental QPO is seen in $3 - 40$ keV energy band and the harmonic ceases to exist beyond ~ 20 keV.

ACKNOWLEDGEMENTS

Authors thank the anonymous reviewers for constructive comments and useful suggestions that help to improve the quality of the manuscript. AU and SD thank the Department of Physics, IIT Guwahati, for providing the facilities to complete this work. AU, SD, and AN acknowledge the support from ISRO sponsored project (DS_2B-13013(2)/5/2020-Sec.2). AN also thanks GH, SAG; DD, PDMSA; Associate Director and Director, URSC for encouragement and continuous support to carry out this research. This work uses data from the *AstroSat* mission of the ISRO archived at the Indian Space Science Data Centre (ISSDC). This work has used the data from the Soft X-ray Telescope (SXT) developed at TIFR, Mumbai, and the SXT POC at TIFR is thanked for verifying and releasing the data and providing the necessary software tools. This work has also used the data from the LAXPC Instruments developed at TIFR, Mumbai, and the LAXPC POC at TIFR is thanked for verifying and releasing the data. This publication also made use of data from the *NuSTAR* mission by the National Aeronautics and Space Administration. This work has also used data from Monitor of All-sky X-ray Image (*MAXI*) data provided by Institute of Physical and Chemical Research (RIKEN), Japan Aerospace Exploration Agency (JAXA), and the *MAXI* team. Also this research made use of software provided by the High Energy Astrophysics Science Archive Research Center (HEASARC) and NASA’s Astrophysics Data System Bibliographic Services.

DATA AVAILABILITY

Data used for this publication are currently available at the *AstroSat* ISSDC website (https://astrobrowse.issdc.gov.in/astro_archive/archive), *MAXI* websites (<http://maxi.riken.jp/top/index.html>) and *NuSTAR* data at HEASARC (<https://heasarc.gsfc.nasa.gov/docs/archive.html>).

REFERENCES

- Agrawal P. C., 2001, in Inoue H., Kunieda H., eds, Astronomical Society of the Pacific Conference Series Vol. 251, New Century of X-ray Astronomy. p. 512
- Agrawal V. K., Nandi A., Girish V., Ramadevi M. C., 2018, *MNRAS*, **477**, 5437
- Alabarta K., et al., 2021, *MNRAS*, **507**, 5507
- Alam M. S., Dewangan G. C., Belloni T., Mukherjee D., Jhingan S., 2014, *MNRAS*, **445**, 4259
- Altamirano D., Strohmayer T., 2012, *ApJ*, **754**, L23
- Aneesha U., Mandal S., 2020, *A&A*, **637**, A47
- Aneesha U., Mandal S., Sreehari H., 2019, *MNRAS*, **486**, 2705
- Antia H. M., et al., 2017, *ApJS*, **231**, 10
- Antia H. M., et al., 2021, *Journal of Astrophysics and Astronomy*, **42**, 32
- Antia H. M., Agrawal P. C., Katoch T., Manchanda R. K., Mukerjee K., Shah P., 2022, *ApJS*, **260**, 40
- Arnaud K. A., 1996, in Jacoby G. H., Barnes J., eds, Astronomical Society of the Pacific Conference Series Vol. 101, Astronomical Data Analysis Software and Systems V. p. 17
- Athulya M. P., Nandi A., 2023, *MNRAS*, **525**, 489
- Athulya M. P., Radhika D., Agrawal V. K., Ravishankar B. T., Naik S., Mandal S., Nandi A., 2022, *MNRAS*, **510**, 3019
- Baby B. E., Bhuvana G. R., Radhika D., Katoch T., Mandal S., Nandi A., 2021, *MNRAS*, **508**, 2447
- Belloni T., 2005, in Burderi L., Antonelli L. A., D’Antona F., di Salvo T., Israel G. L., Piersanti L., Tornambè A., Straniero O., eds, American Institute of Physics Conference Series Vol. 797, Interacting Binaries: Accretion, Evolution, and Outcomes. pp 197–204 ([arXiv:astro-ph/0504185](https://arxiv.org/abs/astro-ph/0504185)), doi:[10.1063/1.2130233](https://doi.org/10.1063/1.2130233)
- Belloni T., Hasinger G., 1990, *A&A*, **230**, 103
- Belloni T. M., Motta S. E., 2016, in Bambi C., ed., Astrophysics and Space Science Library Vol. 440, Astrophysics of Black Holes: From Fundamental Aspects to Latest Developments. p. 61 ([arXiv:1603.07872](https://arxiv.org/abs/1603.07872)), doi:[10.1007/978-3-662-52859-4_2](https://doi.org/10.1007/978-3-662-52859-4_2)
- Belloni T., Klein-Wolt M., Méndez M., van der Klis M., van Paradijs J., 2000, *A&A*, **355**, 271
- Belloni T., Homan J., Casella P., van der Klis M., Nespoli E., Lewin W. H. G., Miller J. M., Méndez M., 2005, *A&A*, **440**, 207
- Bhowmick R., Debnath D., Chatterjee K., Nagarkoti S., Chakrabarti S. K., Sarkar R., Chatterjee D., Jana A., 2021, *ApJ*, **910**, 138
- Bhuvana G. R., Radhika D., Agrawal V. K., Mandal S., Nandi A., 2021, *MNRAS*, **501**, 5457
- Bhuvana G. R., Radhika D., Nandi A., 2022, *Advances in Space Research*, **69**, 483
- Bradley C. K., Hynes R. I., Kong A. K. H., Haswell C. A., Casares J., Gallo E., 2007, *ApJ*, **667**, 427
- Capitanio F., Ubertini P., Bazzano A., Del Santo M., 2010, in The First Year of MAXI: Monitoring Variable X-ray Sources. p. 11
- Casella P., Belloni T., Stella L., 2005, *ApJ*, **629**, 403
- Chakrabarti S. K., 1990, Theory of Transonic Astrophysical Flows, doi:[10.1142/1091](https://doi.org/10.1142/1091).
- Chakrabarti S. K., Manickam S. G., 2000, *ApJ*, **531**, L41
- Chakrabarti S., Titarchuk L. G., 1995, *ApJ*, **455**, 623
- Chakrabarti S. K., Debnath D., Nandi A., Pal P. S., 2008, *A&A*, **489**, L41
- Chakrabarti S. K., Debnath D., Nagarkoti S., 2019, *Advances in Space Research*, **63**, 3749
- Chand S., Agrawal V. K., Dewangan G. C., Tripathi P., Thakur P., 2020, *ApJ*, **893**, 142
- Chand S., Agrawal V. K., Dewangan G. C., Tripathi P., Thakur P., 2021, *Journal of Astrophysics and Astronomy*, **42**, 38
- Chatterjee R., Agrawal V. K., Nandi A., 2021, *MNRAS*, **505**, 3785
- Chaty S., Muñoz Arjonilla A. J., Dubus G., 2015, *A&A*, **577**, A101
- Chen W., Shrader C. R., Livio M., 1997, *ApJ*, **491**, 312
- Chen Y. P., Zhang S., Torres D. F., Wang J. M., Li J., Li T. P., Qu J. L., 2010, *A&A*, **522**, A99
- Corbel S., Nowak M. A., Fender R. P., Tzioumis A. K., Markoff S., 2003, *A&A*, **400**, 1007

- Corbel S., Tomsick J. A., Kaaret P., 2006, *ApJ*, **636**, 971
- Corral-Santana J. M., Casares J., Muñoz-Darias T., Bauer F. E., Martínez-Pais I. G., Russell D. M., 2016, *A&A*, **587**, A61
- Das S., Chattopadhyay I., Nandi A., Molteni D., 2014, *MNRAS*, **442**, 251
- Debnath D., Chakrabarti S. K., Nandi A., 2010, *A&A*, **520**, A98
- Debnath D., Chakrabarti S. K., Nandi A., 2013, *Advances in Space Research*, **52**, 2143
- Debnath D., Chatterjee K., Nath S. K., Chang H.-K., Bhowmick R., 2023, *Advances in Space Research*, **71**, 3508
- Del Santo M., et al., 2009, *MNRAS*, **392**, 992
- Dong A.-J., Liu C., Ge K., Liu X., Zhi Q.-J., You Z.-Y., 2021, *Frontiers in Astronomy and Space Sciences*, **8**, 37
- Dzięlał M. A., Zdziarski A. A., Szanecki M., De Marco B., Niedźwiecki A., Markowitz A., 2019, *MNRAS*, **485**, 3845
- Ebisawa K., Titarchuk L., Chakrabarti S. K., 1996, *PASJ*, **48**, 59
- Fender R. P., Homan J., Belloni T. M., 2009, *MNRAS*, **396**, 1370
- Frank J., King A., Raine D. J., 2002, *Accretion Power in Astrophysics: Third Edition*. Cambridge University Press
- García J. A., et al., 2019, *ApJ*, **885**, 48
- Gehrels N., et al., 2004, *ApJ*, **611**, 1005
- Hameury J. M., Lasota J. P., 2014, *A&A*, **569**, A48
- Hameury J. M., King A. R., Lasota J. P., 1986, *A&A*, **162**, 71
- Harrison F. A., et al., 2013, *ApJ*, **770**, 103
- Heida M., Jonker P. G., Torres M. A. P., Chiavassa A., 2017, *ApJ*, **846**, 132
- Homan J., Belloni T., 2005, *Ap&SS*, **300**, 107
- Homan J., Wijnands R., van der Klis M., Belloni T., van Paradijs J., Klein-Wolt M., Fender R., Méndez M., 2001, *ApJS*, **132**, 377
- Homan J., Miller J. M., Wijnands R., Steeghs D., Belloni T., van der Klis M., Lewin W. H. G., 2003, *The Astronomer's Telegram*, **162**, 1
- Homan J., Miller J. M., Wijnands R., van der Klis M., Belloni T., Steeghs D., Lewin W. H. G., 2005a, *ApJ*, **623**, 383
- Homan J., Buxton M., Markoff S., Bailyn C. D., Nespoli E., Belloni T., 2005b, *ApJ*, **624**, 295
- Husain N., Misra R., Sen S., 2022, *MNRAS*, **510**, 4040
- Husain N., Garg A., Misra R., Sen S., 2023, *MNRAS*, **525**, 4515
- Hynes R. I., Steeghs D., Casares J., Charles P. A., O'Brien K., 2003, *ApJ*, **583**, L95
- Hynes R. I., Steeghs D., Casares J., Charles P. A., O'Brien K., 2004, *ApJ*, **609**, 317
- Ingram A. R., Motta S. E., 2019, *New Astron. Rev.*, **85**, 101524
- Ingram A., Done C., Fragile P. C., 2009, *MNRAS*, **397**, L101
- Iyer N., Nandi A., Mandal S., 2015, *ApJ*, **807**, 108
- Jana A., Chatterjee D., Chang H.-K., Naik S., Mondal S., 2024, *MNRAS*, **527**, 2128
- Kalemci E., Tomsick J. A., Rothschild R. E., Pottschmidt K., Corbel S., Kaaret P., 2006, *ApJ*, **639**, 340
- Kara E., et al., 2019, *Nature*, **565**, 198
- Katoch T., Baby B. E., Nandi A., Agrawal V. K., Antia H. M., Mukerjee K., 2021, *MNRAS*, **501**, 6123
- King A. R., Ritter H., 1998, *MNRAS*, **293**, L42
- Kong A. K. H., Kuulkers E., Charles P. A., Homer L., 2000, *MNRAS*, **312**, L49
- Kong L. D., et al., 2020, *Journal of High Energy Astrophysics*, **25**, 29
- Krimm H. A., et al., 2013, *ApJS*, **209**, 14
- Kushwaha A., Agrawal V. K., Nandi A., 2021, *MNRAS*, **507**, 2602
- Kylafis N. D., Reig P., Papadakis I., 2020, *A&A*, **640**, L16
- Lasota J.-P., 2001, *New Astron. Rev.*, **45**, 449
- Laurent P., Titarchuk L., 2011, *ApJ*, **727**, 34
- Leahy D. A., Darbro W., Elsner R. F., Weisskopf M. C., Sutherland P. G., Kahn S., Grindlay J. E., 1983, *ApJ*, **266**, 160
- Lightman A. P., Zdziarski A. A., 1987, *ApJ*, **319**, 643
- Liu H., Zhang L., Tao L., Chen Y., Qu J., Zhang S., Zhang S.-n., 2021, *The Astronomer's Telegram*, **14504**, 1
- Liu H., Jiang J., Zhang Z., Bambi C., Ji L., Kong L., Zhang S., 2022, *MNRAS*, **513**, 4308
- Lucchini M., et al., 2023, *ApJ*, **958**, 153
- Maccarone T. J., 2003, *A&A*, **409**, 697
- Majumder S., Sreehari H., Aftab N., Katoch T., Das S., Nandi A., 2022, *MNRAS*, **512**, 2508
- Makishima K., Maejima Y., Mitsuda K., Bradt H. V., Remillard R. A., Tuohy I. R., Hoshi R., Nakagawa M., 1986, *ApJ*, **308**, 635
- Merkert T. H., Canizares C. R., Clark G. W., Lewin W. H. G., Schnopper H. W., Sprott G. F., 1973, *ApJ*, **184**, L67
- Matsuoka M., et al., 2009, *PASJ*, **61**, 999
- McClintock J. E., Remillard R. A., 2006, in , Vol. 39, *Compact stellar X-ray sources*. pp 157–213, doi:10.48550/arXiv.astro-ph/0306213
- Méndez M., van der Klis M., 1997, *ApJ*, **479**, 926
- Mitsuda K., et al., 1984, *PASJ*, **36**, 741
- Miyamoto S., Kitamoto S., Hayashida K., Egoshi W., 1995, *ApJ*, **442**, L13
- Molla A. A., Chakrabarti S. K., Debnath D., Mondal S., 2017, *ApJ*, **834**, 88
- Molteni D., Sponholz H., Chakrabarti S. K., 1996, *ApJ*, **457**, 805
- Mondal S., Salgundi A., Chatterjee D., Jana A., Chang H. K., Naik S., 2023, *MNRAS*, **526**, 4718
- Motta S., Muñoz-Darias T., Casella P., Belloni T., Homan J., 2011, *MNRAS*, **418**, 2292
- Muñoz-Darias T., Casares J., Martínez-Pais I. G., 2008, *MNRAS*, **385**, 2205
- Nakahira S., et al., 2012, *PASJ*, **64**, 13
- Nandi A., Manickam S. G., Rao A. R., Chakrabarti S. K., 2001, *MNRAS*, **324**, 267
- Nandi A., Debnath D., Mandal S., Chakrabarti S. K., 2012, *A&A*, **542**, A56
- Nandi A., et al., 2018, *Ap&SS*, **363**, 90
- Nandi A., Das S., Majumder S., Katoch T., Antia H. M., Shah P., 2024, *MNRAS*, **531**, 1149
- Paice J. A., Gandhi P., Pahari M., 2019, *The Astronomer's Telegram*, **12413**, 1
- Parker M. L., et al., 2016, *ApJ*, **821**, L6
- Peirano V., Méndez M., García F., Belloni T., 2023, *MNRAS*, **519**, 1336
- Plant D. S., Fender R. P., Ponti G., Muñoz-Darias T., Coriat M., 2014, *MNRAS*, **442**, 1767
- Plotkin R. M., Gallo E., Jonker P. G., 2013, *ApJ*, **773**, 59
- Prabhakar G., Mandal S., Athulya M. P., Nandi A., 2022, *MNRAS*, **514**, 6102
- Radhika D., Nandi A., 2014, *Advances in Space Research*, **54**, 1678
- Radhika D., Nandi A., Agrawal V. K., Mandal S., 2016, *MNRAS*, **462**, 1834
- Radhika D., Sreehari H., Nandi A., Iyer N., Mandal S., 2018, *Ap&SS*, **363**, 189
- Remillard R. A., McClintock J. E., 2006, *ARA&A*, **44**, 49
- Remillard R. A., Sobczak G. J., Munro M. P., McClintock J. E., 2002, *ApJ*, **564**, 962
- Remillard R. A., McClintock J. E., Orosz J. A., Levine A. M., 2006, *ApJ*, **637**, 1002
- Seifina E., Titarchuk L., 2010, *ApJ*, **722**, 586
- Seifina E., Titarchuk L., Shaposhnikov N., 2014, *ApJ*, **789**, 57
- Shahbaz T., Charles P. A., King A. R., 1998, *Soft X-Ray Transient Light Curves as Standard Candles: Exponential Versus Linear Decays*, Technical Report, OUAST/98/13 Dept. of Astrophysics
- Shaposhnikov N., Titarchuk L., 2009, *ApJ*, **699**, 453
- Sreehari H., Nandi A., 2021, *MNRAS*, **502**, 1334
- Sreehari H., Nandi A., Radhika D., Iyer N., Mandal S., 2018, *Journal of Astrophysics and Astronomy*, **39**, 5
- Sreehari H., Iyer N., Radhika D., Nandi A., Mandal S., 2019a, *Advances in Space Research*, **63**, 1374
- Sreehari H., Ravishankar B. T., Iyer N., Agrawal V. K., Katoch T. B., Mandal S., Nandi A., 2019b, *MNRAS*, **487**, 928
- Sreehari H., Nandi A., Das S., Agrawal V. K., Mandal S., Ramadevi M. C., Katoch T., 2020, *MNRAS*, **499**, 5891
- Sridhar N., García J. A., Steiner J. F., Connors R. M. T., Grinberg V., Harrison F. A., 2020, *ApJ*, **890**, 53
- Steiner J. F., McClintock J. E., Reid M. J., 2012, *ApJ*, **745**, L7
- Stella L., Vietri M., 1998, *ApJ*, **492**, L59
- Stella L., Vietri M., Morsink S. M., 1999, *ApJ*, **524**, L63
- Stiele H., Kong A. K. H., 2021a, *ApJ*, **914**, 93
- Stiele H., Kong A. K. H., 2021b, *ApJ*, **914**, 93
- Stiele H., Yu W., 2016, *MNRAS*, **460**, 1946
- Sunyaev R. A., Titarchuk L. G., 1980, *A&A*, **86**, 121
- Tagger M., Pellat R., 1999, *A&A*, **349**, 1003

- Tanaka Y., Lewin W. H. G., 1995, in X-ray Binaries. pp 126–174
- Tetarenko B. E., Sivakoff G. R., Heinke C. O., Gladstone J. C., 2016, *ApJS*, **222**, 15
- Titarchuk L., 1994, *ApJ*, **434**, 570
- Titarchuk L., Lyubarskij Y., 1995, *ApJ*, **450**, 876
- Titarchuk L., Osherovich V., 1999, *ApJ*, **518**, L95
- Titarchuk L., Osherovich V., 2000, *ApJ*, **542**, L111
- Titarchuk L., Seifina E., 2009, *ApJ*, **706**, 1463
- Titarchuk L., Seifina E., 2017, *A&A*, **602**, A113
- Titarchuk L., Seifina E., 2021, *MNRAS*, **501**, 5659
- Tomsick J. A., et al., 2008, *ApJ*, **680**, 593
- Tursunov A. A., Kološ M., 2018, *Physics of Atomic Nuclei*, **81**, 279
- Wang-Ji J., et al., 2018, *ApJ*, **855**, 61
- Wang J., et al., 2020, *ApJ*, **899**, 44
- Wang P. J., et al., 2022a, *MNRAS*, **512**, 4541
- Wang J., et al., 2022b, *ApJ*, **930**, 18
- Wijnands R., Homan J., van der Klis M., 1999, *ApJ*, **526**, L33
- Wilms J., Allen A., McCray R., 2000, *ApJ*, **542**, 914
- Yadav J. S., et al., 2016, in den Herder J.-W. A., Takahashi T., Bautz M., eds, Society of Photo-Optical Instrumentation Engineers (SPIE) Conference Series Vol. 9905, Space Telescopes and Instrumentation 2016: Ultraviolet to Gamma Ray. p. 99051D, doi:10.1117/12.2231857
- Zdziarski A. A., Johnson W. N., Magdziarz P., 1996, *MNRAS*, **283**, 193
- Zdziarski A. A., Gierliński M., Mikołajewska J., Wardziński G., Smith D. M., Harmon B. A., Kitamoto S., 2004, *MNRAS*, **351**, 791
- Zhang L., Wang Y., Méndez M., Chen L., Qu J., Altamirano D., Belloni T., 2017, *ApJ*, **845**, 143
- Życki P. T., Done C., Smith D. A., 1999, *MNRAS*, **309**, 561
- van Paradijs J., 1996, *ApJ*, **464**, L139
- van der Klis M., 1989, *ARA&A*, **27**, 517

This paper has been typeset from a $\text{\TeX}/\text{\LaTeX}$ file prepared by the author.